AGU PUBLICATIONS

Tectonics

RESEARCH ARTICLE
10.1002/2014TC003593

Key Points:
- The Leo Pargil shear zone exhumed midcrustal rocks during W directed shearing
- Extension potentially occurred in a system dominated by radial extension

Correspondence to:
J. M. Langille,
jlangill@unca.edu

Citation:
Langille, J. M., M. J. Jessup, J. Cottle, and T. Ahmad (2014), Kinematic and thermal studies of the Leo Pargil Dome: Implications for synconvergent extension in the NW Indian Himalaya, *Tectonics*, *33*, 1766–1786, doi:10.1002/2014TC003593.

Received 19 MAR 2014
Accepted 20 AUG 2014
Accepted article online 23 AUG 2014
Published online 24 SEP 2014

Kinematic and thermal studies of the Leo Pargil Dome: Implications for synconvergent extension in the NW Indian Himalaya

J. M. Langille[1], M. J. Jessup[1], J. Cottle[2], and T. Ahmad[3]

[1]Department of Earth and Planetary Sciences, University of Tennessee, Knoxville, Knoxville, Tennessee, USA, [2]Department of Earth Science, University of California, Santa Barbara, California, USA, [3]Department of Geology, University of Delhi, Delhi, India

Abstract Building of the Himalaya and Tibetan Plateau involved an interplay between crustal thickening and extension. The NW Indian Himalaya near the Leo Pargil dome contains approximately N trending brittle normal faults and NE trending normal-sense shear zones (i.e., bounding Leo Pargil dome) between the South Tibetan detachment system to the south and the Karakoram fault to the north. The Leo Pargil shear zone bounds the southwest flank of the Leo Pargil dome. Estimates of deformation temperatures and mean kinematic vorticity (W_m) from the shear zone were integrated with pressure-temperature estimates to evaluate its kinematic and thermal evolution. Oblique quartz fabrics yielded kinematic vorticity estimates indicating that the rocks within the shear zone were thinned by up to 62% during W directed shearing. Top-down-to-the-W ductile deformation is recorded at temperatures from >650°C at the deepest structural levels within the dome and from 400 to 500°C at shallower structural depths. Hanging wall rocks record much lower temperatures. Pressure-temperature data indicate that rocks in the dome were exhumed from depths of ~36 to 22 km. In contrast to other mechanisms proposed for dome formation across the Himalaya, initiation of ductile movement on the Leo Pargil shear zone occurred at midcrustal levels in a region of localized synconvergent extension at >23 Ma. The timing and kinematic setting of deformation on the Leo Pargil shear zone suggest that exhumation could be related to a localized zone of transtension near the Karakoram fault zone.

1. Introduction

Continental collision between the Indian and Eurasian plates since the Eocene [e.g., *Searle et al*., 1987; *Najman et al*., 2010] resulted in the Himalaya and the Tibetan Plateau by a combination of crustal shortening and extension. A network of thrust faults, strike-slip faults, and normal faults accommodates shortening and extension within the Himalaya and Tibetan Plateau (Figure 1) [e.g., *Molnar and Tapponier*, 1975, 1978; *Jouanne et al*., 2004; *Styron et al*., 2011]. The geodetic convergence rate between the Indian and Eurasian plates varies across the orogen, with ~35 mm/yr between the Indian and Eurasian plates in the Nepalese Himalaya [*Bettinelli et al*., 2006] and higher rates along the eastern 200 km of the range [*Banerjee et al*., 2008]. The Main Frontal thrust accommodated ~20 mm/yr (Holocene slip rate) during NE directed shortening focused along the Himalayan front [*Wesnousky et al*., 1999; *Lavé and Avouac*, 2000], while the remainder is transferred to strike-slip faults in the Tibetan Plateau and normal faults within the Himalaya and the Tibetan Plateau (Figure 1) [*Styron et al*., 2011]. Greater than 3 mm/yr is accommodated by normal faults across the Himalayan front and the southern Tibetan Plateau [*Styron et al*., 2011].

The arc-parallel Main Central thrust zone (MCTZ) and the South Tibetan detachment system (STDS) are major structures exposed along the Himalaya that were active until the middle Miocene [also see *Catlos et al*., 2001; *Kellett et al*., 2009] to accommodate convergence between the Indian and Asian plates [*Grujic et al*., 1996, 2002; *Grasemann et al*., 1999; *Vannay and Grasemann*, 2001; *Vannay et al*., 2004; *Searle et al*., 2006]. After the bulk of deformation on the STDS and MCTZ ended [e.g., *Gansser*, 1981], NE directed convergence was accommodated by other arc-parallel thrust faults south of the MCTZ and arc-perpendicular normal faults and shear zones (beginning at ~18–13 Ma in the central Himalaya) [*Coleman and Hodges*, 1995; *Williams et al*., 2001; *Jessup and Cottle*, 2010].

In the central Himalaya, normal faults and shear zones such as the Ama Drime detachment, Dinggyê graben, Tingri graben, and the Thakkola graben record a transition to orogen-parallel extension after the cessation of movement on the STDS and MCTZ [e.g., *Kapp and Guynn*, 2004; *Jessup et al*., 2008; *Jessup and Cottle*, 2010; *Lee et al*., 2011].

©2014. American Geophysical Union. All Rights Reserved.

19449194, 2014, 9, Downloaded from https://agupubs.onlinelibrary.wiley.com/doi/10.1002/2014TC003593 by National Medical Library The Director, Wiley Online Library on [21/11/2022]. See the Terms and Conditions (https://onlinelibrary.wiley.com/terms-and-conditions) on Wiley Online Library for rules of use; OA articles are governed by the applicable Creative Commons License

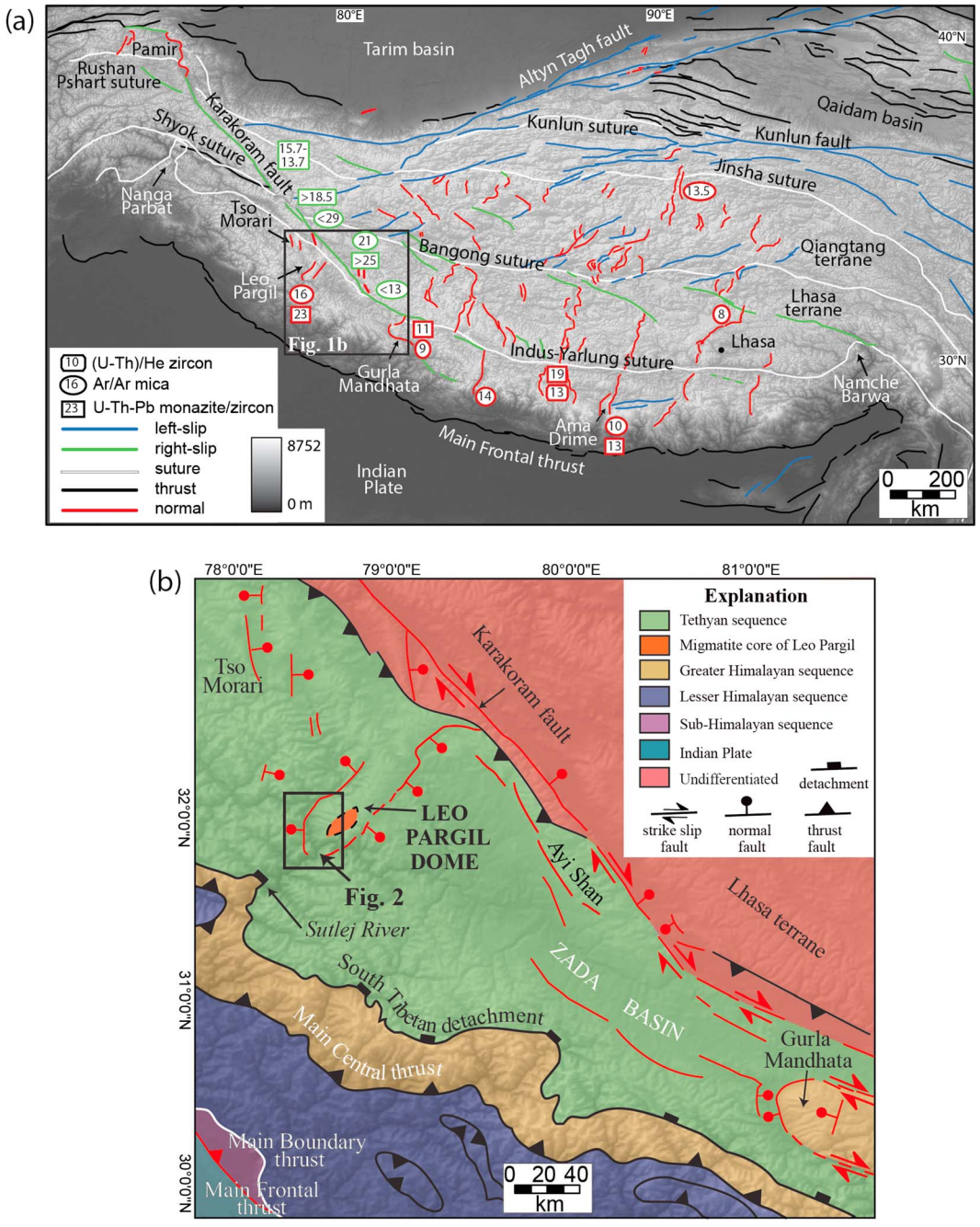

Figure 1. (a) Active faults and suture zones in the Himalaya overlain on a digital elevation model of the Himalaya and Tibetan Plateau. Faults modified after *Taylor and Yin* [2009]. Numbers are ages (Ma) for normal or strike-slip fault initiation [*Coleman and Hodges*, 1995; *Harrison et al.*, 1995; *Murphy et al.*, 2000; *Blisniuk et al.*, 2001; *Murphy et al.*, 2002; *de Sigoyer et al.*, 2004; *Lacassin et al.*, 2004a; *Phillips et al.*, 2004; *Phillips and Searle*, 2007; *Thiede et al.*, 2006; *Valli et al.*, 2007; *Kali et al.*, 2010; *Lee et al.*, 2011; *Leloup et al.*, 2011; *Mitsuishi et al.*, 2012; *Langille et al.*, 2012]. (b) Simplified geologic map of the western Himalaya [*Vannay and Grasemann*, 2001; *Murphy et al.*, 2002; *Thiede et al.*, 2006; *Valli et al.*, 2007]. Active structures are in red.

E-W extension across the Tibetan Plateau is partitioned along sets of conjugate strike-slip faults that contain left-lateral strike-slip faults throughout the northern Tibetan Plateau and on right-lateral strike-slip faults throughout the southern Tibetan Plateau. Normal faults and shear zones occur throughout the Himalayan front and the Tibetan Plateau (Figure 1) [e.g., *Molnar and Tapponier*, 1975, 1978; *Taylor et al.*, 2003; *Hintersberger et al.*, 2010, 2011; *Styron et al.*, 2011]. Normal faults that accommodated orogen-parallel extension in the central

©2014. American Geophysical Union. All Rights Reserved.

19449194, 2014, 9, Downloaded from https://agupubs.onlinelibrary.wiley.com/doi/10.1002/2014TC003593 by National Medical Library The Director, Wiley Online Library on [21/11/2022]. See the Terms and Conditions (https://onlinelibrary.wiley.com/terms-and-conditions) on Wiley Online Library for rules of use; OA articles are governed by the applicable Creative Commons License

19449194, 2014, 9, Downloaded from https://agupubs.onlinelibrary.wiley.com/doi/10.1002/2014TC003593 by National Medical Library The Director, Wiley Online Library on [21/11/2022]. See the Terms and Conditions (https://onlinelibrary.wiley.com/terms-and-conditions) on Wiley Online Library for rules of use; OA articles are governed by the applicable Creative Commons License

Himalaya are potentially part of a similar kinematic setting as strike-slip faults and graben in the Tibetan Plateau (Figure 1a) [*Armijo et al*., 1986; *Taylor et al*., 2003; *Kapp and Guynn*, 2004; *Jessup and Cottle*, 2010].

From west to east throughout the Himalaya and Tibetan Plateau, the trend of normal faults radiate between NW to NE, potentially due to collisional stresses resulting from convergence [*Kapp and Guynn*, 2004]. In the central Himalaya, shear zones and normal faults trend perpendicular to the Himalayan front (e.g., Ama Drime detachment, Dinggyê graben, Tingri graben, and the Thakkola graben). These normal faults and shear zones align with the radial pattern across the Himalaya. In the NW Himalaya, NE trending normal faults that bound the Leo Pargil dome (LPD) are likewise oriented perpendicular to the orogenic front but do not follow this radial pattern, suggesting that the kinematic history of extension here may have some differences compared to the central Himalaya (Figure 1) [*Hintersberger et al*., 2010, 2011].

The LPD and Gurla Mandhata dome, located in the western Himalaya, were exhumed along arc-perpendicular normal-sense shear zones (Figure 1) [*Murphy et al*., 2000, 2002; *Thiede et al*., 2006; *Langille et al*., 2012], and they are thought to extend into the Karakoram fault system. Beginning in the late Miocene, the Gurla Mandhata detachment records W directed extension that was kinematically linked to dextral displacement on the Karakoram fault system [e.g., *Murphy et al*., 2002]. The Leo Pargil shear zone (LPSZ) bounds the southwest side of the LPD [*Thiede et al*., 2006], and synkinematic monazite ages constrain the initiation of ductile, W directed displacement to $>$23 Ma [*Langille et al*., 2012].

Despite the widely debated ages for initiation of the Karakoram fault [e.g., *Lacassin et al*., 2004a, 2004b; *Searle and Phillips*, 2004; *Phillips and Searle*, 2007], previous studies provide elegant models for the kinematic relationships between NE trending shear zones that bound the LPD, N trending brittle normal faults near the dome, and the Karakoram fault system [*Ni and Barazangi*, 1985; *Thiede et al*., 2006; *Hintersberger et al*., 2010, 2011]. However, aside from the pioneering efforts documenting the kinematics and timing of movement on the LPSZ using $^{40}Ar/^{39}Ar$ data [*Thiede et al*., 2006], relatively little constraints exist for the tectonic significance of W directed synconvergent extension at $>$23 Ma [*Langille et al*., 2012] or the thermal and kinematic evolution of the LPSZ before the formation of the N trending brittle normal faults.

To constrain the kinematic evolution of the LPSZ, through combined kinematic and thermobarometric studies, structural data and rock samples were collected from the LPD and the hanging wall of the LPSZ. Thin sections of representative deformed samples from the LPSZ were analyzed using quartz and feldspar recrystallization textures, mean kinematic vorticity, and pressure-temperature (P-T) estimates. These methods constrain the temperature at which the samples were deformed, the kinematics during deformation, and the temperature and pressure reached by the rocks during prograde metamorphism. These data are used to constrain the thermal and kinematic evolution of the LPSZ and are combined with existing data sets from the NW Himalaya to evaluate models for synconvergent extension in the Leo Pargil region and mechanisms for gneiss dome exhumation.

2. Regional Geology

In the southern Sutlej Valley, the Main Boundary thrust and Main Frontal thrust are present in the footwall of the MCTZ [e.g., *Vannay and Grasemann*, 2001]. To the north, the Greater Himalayan Sequence (GHS) is exposed between the MCTZ and the STDS (Figure 1b) [e.g., *Vannay and Grasemann*, 2001]. In the NW Indian Himalaya, the ductile Sangla detachment and the Zanskar shear zone [*Herren*, 1987; *Dézes et al*., 1999] constitute segments of the STDS. The GHS is composed of Neoproterozoic to Cambrian rocks that record metamorphism and anatexis in the early to middle Miocene and were exhumed by the MCTZ and STDS [e.g., *Vannay and Grasemann*, 2001]. The Lesser Himalayan sequence underlies the GHS, structurally beneath the MCTZ (Figure 1b). The Tethyan Sedimentary sequence (TSS) structurally overlies the GHS. The base of the TSS, above the Sangla detachment in the northern Sutlej Valley, is composed of the Lower Proterozoic to Cambrian metasedimentary rocks of the Haimanta Group [*Frank et al*., 1995; *Vannay and Grasemann*, 2001; *Wiesmayr and Grasemann*, 2002; *Chambers et al*., 2009]. Alternatively, the Haimanta Group has also been included as part of the GHS rather than the TSS [*Searle et al*., 2007]. The base of the Haimanta Group is intruded by the 488 Ma Akpa (also termed "Kinnaur Kailas") granite [*Miller et al*., 2001].

North from the Akpa granite, the N dipping Haimanta Group preserves a decrease in metamorphic grade up section, from the kyanite-isograd exposed structurally above the Akpa granite to the biotite-isograd

©2014. American Geophysical Union. All Rights Reserved.

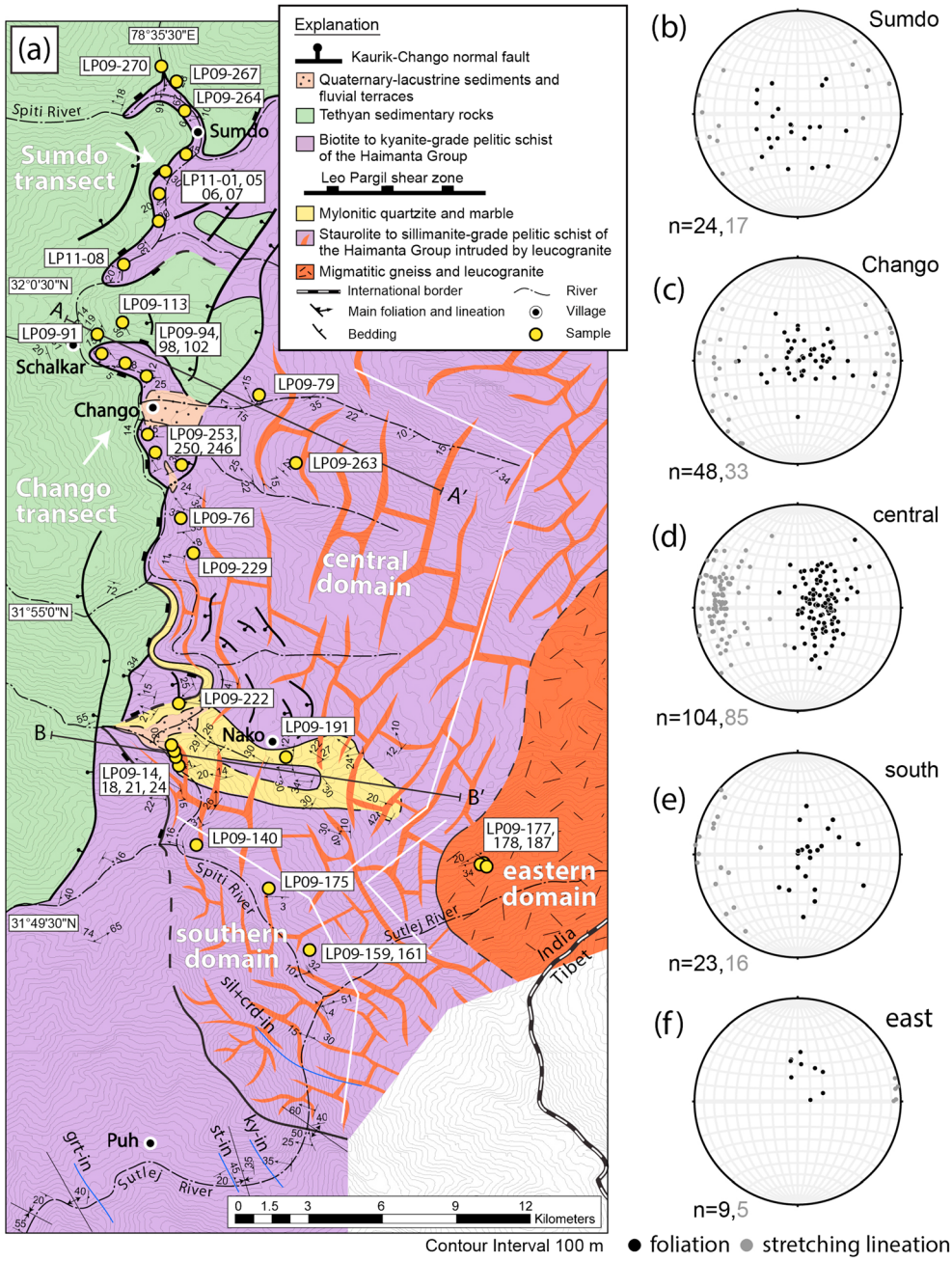

Figure 2. (a) Geologic map of the southern end of the Leo Pargil dome from *Langille et al.* [2012]. See Figure 1b for location. Refer to Figure 3 for cross sections: grt, garnet; st; staurolite; ky, kyanite; sil, sillimanite; crd, cordierite. (b–f) Main foliation and stretching lineation data for each domain: *n*, number of data points.

approximately 6 km up section [*Chambers et al.*, 2009]. The Haimanta Group transitions to S dipping at the southern end of the LPD (Figure 2). The Haimanta Group at the staurolite-isograd (Figure 2), just south of the dome, reached peak conditions of ~600°C and 7 kbar during Barrovian metamorphism [M. Jessup et al., Crustal thickening, Barrovian metamorphism, and exhumation of mid-crustal rocks along inherited structures: Insights from the Himalaya, NW India, *Tectonics*, in review, 2014; *Langille et al.*, 2012]. Prograde metamorphism in the Haimanta Group in the Sutlej Valley began at >34 Ma, with peak burial at 30 Ma and garnet growth ending by 28 Ma [*Chambers et al.*, 2009]. Staurolite and kyanite growth ceased at ~30 Ma [*Langille et al.*, 2012]. The Haimanta Group in the Sutlej Valley contains primary structures such as cross beds and graded bedding that are deformed by folds [*Chambers et al.*, 2009; M. Jessup et al., in review, 2014]. The top of the Haimanta Group is

©2014. American Geophysical Union. All Rights Reserved.

19449194, 2014, 9, Downloaded from https://agupubs.onlinelibrary.wiley.com/doi/10.1002/2014TC003593 by National Medical Library The Director, Wiley Online Library on [21/11/2022]. See the Terms and Conditions (https://onlinelibrary.wiley.com/terms-and-conditions) on Wiley Online Library for rules of use; OA articles are governed by the applicable Creative Commons License

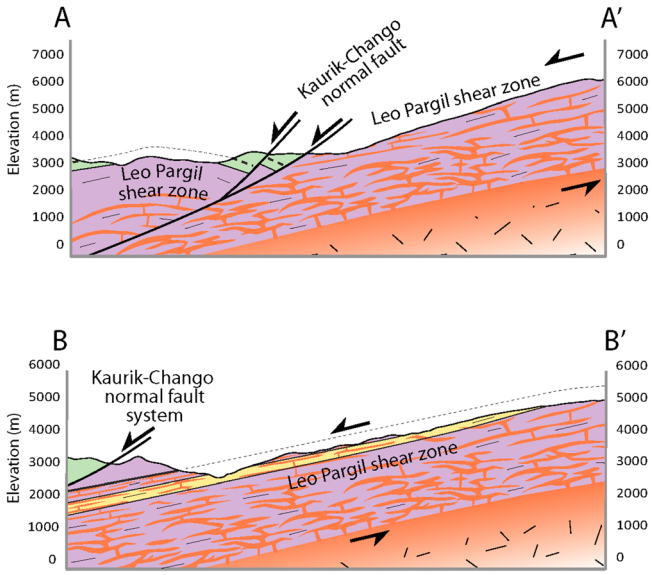

Figure 3. Cross sections through A-A′ and B-B′ of Figure 2. From *Langille et al*. [2012].

separated from the overlying Ordovician to Jurassic sedimentary rocks of the TSS (e.g., Shian, Pin, and Muth Formations) by an unconformity [*Wiesmayr and Grasemann*, 2002].

Active faulting across the Himalaya records NE-SW shortening focused along the southern margin of the Himalaya, E-W extension within the Himalaya and Tibetan Plateau, and strike-slip faulting in the Tibetan Plateau [*Molnar and Tapponier*, 1975, 1978]. The regional brittle deformation in the NW Indian Himalaya has been characterized by several deformation styles with the following recorded at the LPD [*Hintersberger et al*., 2011]. These events began with ENE-WSW shortening on strike-slip faults presumably related to early onset of the dome (D2), NE-SW arc-normal extension related to the STDS (D3), NW-SE arc-parallel extension (D4), and lastly, E-W extension (D6) [*Hintersberger et al*., 2011]. D5 is not recorded in the Leo Pargil dome. These data are used to support other models in which D4 occurred in response to radial expansion due to southward migration of the active zone of overthrusting and relaxation in the hinterland [*Murphy et al*., 2009]. However, *Hintersberger et al*. [2011] do suggest that NE striking normal faults (D4) within the LPD could have resulted from rotation of E-W extension structures (D6) since 14–16 Ma [*Thiede et al*., 2006; *Hintersberger et al*., 2010]. E-W extension structures (D6) are not limited to the LPD, but occur throughout the NW Indian Himalaya, and they are attributed to ongoing extension in the Tibetan Plateau [*Hintersberger et al*., 2011].

Arc-perpendicular normal-sense shear zones that bound the LPD and Gurla Mandhata dome record localized extension [*Murphy et al*., 2002; *Langille et al*., 2012], and they extend to the dextral Karakoram fault system (Figure 1b). The Karakoram fault extends from the Pamirs in the northwest [e.g., *Robinson et al*., 2007; *Robinson*, 2009] to the normal faults at the Gurla Mandhata detachment in the southeast [*Murphy et al*., 2002]. A splay at the southern extent of the Karakoram fault is interpreted to continue southeast along the Indus-Yarlung suture [*Lacassin et al*., 2004a] (Figure 1a).

3. Geology of the Leo Pargil Dome

The LPD extends northeast to the Ayi Shan, an elongate, NW trending range that is bound by the Karakoram fault system to the NE [*Valli et al*., 2007; *Sanchez et al*., 2010; *Zhang et al*., 2011] (Figure 1). The NE trending, SE directed Qusum detachment fault [*Zhang et al*., 2000] separates the southeastern margin of the dome from the Zada basin [*Murphy et al*., 2009; *Saylor et al*., 2010]. The NE trending, ductile, W directed LPSZ bounds the west flank of the LPD. Faults that extend northeast into the right-lateral Karakoram fault system are interpreted to accommodate orogen-parallel extension (Figures 1–3) [*Ni and Barazangi*, 1985; *Zhang et al*., 2000; *Thiede et al*., 2006; *Hintersberger et al*., 2010]. The Kaurik-Chango brittle normal fault on the west side of the dome offsets the LPSZ (Figures 2 and 3) [*Thiede et al*., 2006].

On the southwest flank of the dome, the LPSZ is a distributed zone of west dipping, amphibolite-facies schist, quartzite, leucogranite, and marble, intruded by several generations of younger leucogranite that was deformed during top-down-to-the-W shearing (Figures 2, 4a, and 4b) [*Thiede et al*., 2006; *Leech*, 2008; *Langille et al*., 2012; *Lederer et al*., 2013]. Biotite schist within the LPD ranges from biotite to garnet grade near Sumdo and Chango, up to sillimanite grade at deeper positions (Figure 2). The schist belongs to the Haimanta Group and records peak Barrovian metamorphism during conditions of ~600–650°C and ~7–8 kbar [*Langille et al*., 2012]. In situ U-Th-Pb metamorphic monazite geochronology constrains peak metamorphism to ~30 Ma [*Langille et al*., 2012].

©2014. American Geophysical Union. All Rights Reserved.

19449194, 2014, 9, Downloaded from https://agupubs.onlinelibrary.wiley.com/doi/10.1002/2014TC003593 by National Medical Library The Director, Wiley Online Library on [21/11/2022]. See the Terms and Conditions (https://onlinelibrary.wiley.com/terms-and-conditions) on Wiley Online Library for rules of use; OA articles are governed by the applicable Creative Commons License

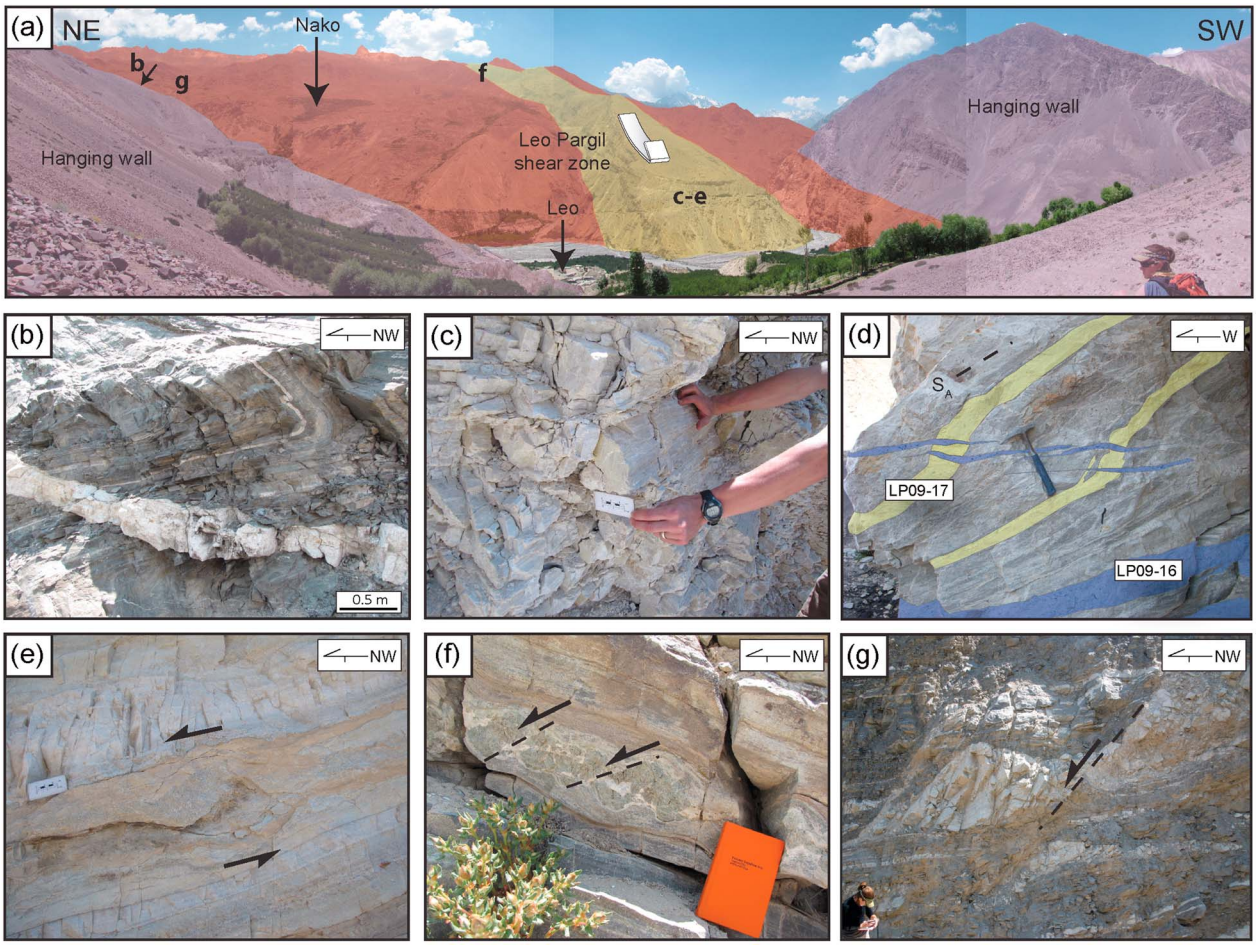

Figure 4. Field photographs from the Leo Pargil dome. (a) A portion of the Leo Pargil shear zone (LPSZ; yellow and red) viewed toward the east. Red corresponds to the Haimanta Group intruded by leucogranite within the dome. Other colors correspond to Figure 2. (b) Deformed and undeformed leucogranites within the LPSZ. Mylonitic quartzite and marble (yellow unit): (c) L-tectonite fabric; (d) LP09-16 is an undeformed leucogranite and LP09-17 is deformed. (e and f) Sheared marble within the quartzite demonstrates top-down-to-the-W shear sense. (g) Sheared leucogranite suggests top-down-to-the-W shear sense.

These metamorphic and timing constraints overlap with data from the Haimanta Group exposed south of the dome in the Sutlej Valley [*Chambers et al.*, 2009]. Top-down-to-the-W shearing overprinted the prograde assemblages. Initiation of extension is recorded by cordierite and sillimanite that replaced staurolite and kyanite during near-isothermal decompression (to ~4 kbar) [*Langille et al.*, 2012]. In situ U-Th-Pb monazite geochronology constrains the onset of ductile, W directed movement to >23 Ma [*Langille et al.*, 2012].

Toward the core of the dome, rocks transition to gneiss and migmatite (Figure 2). A younger generation of leucogranite injected the Haimanta Group and leucogranite within the dome [*Lederer et al.*, 2013]. Near-isothermal decompression during top-down-to-the-W shearing coincident with emplacement of leucogranites from 23 to 18 Ma suggests that decompression potentially induced melting in the core of the dome [*Leech*, 2008; *Langille et al.*, 2012]. Considering that the southwest flank of the dome is composed of deep structural positions of the Haimanta Group, the deeper position toward the core of the dome may contain a component of the GHS.

4. Kinematics and Structure

4.1. Mesoscale Observations

Structural and kinematic data presented by *Thiede et al.* [2006] characterized the western flank of the dome with a shallow W dipping foliation and WNW stretching lineation that has been offset by brittle structures. *Thiede et al.* [2006] proposed four phases of deformation to describe the evolution of these structures in the LPD: D1, which forms the dominant foliation and lineation; D2, millimeter- to meter-scale shear bands that cut the

©2014. American Geophysical Union. All Rights Reserved.

19449194, 2014, 9, Downloaded from https://agupubs.onlinelibrary.wiley.com/doi/10.1002/2014TC003593 by National Medical Library The Director, Wiley Online Library on [21/11/2022]. See the Terms and Conditions (https://onlinelibrary.wiley.com/terms-and-conditions) on Wiley Online Library for rules of use; OA articles are governed by the applicable Creative Commons License

19449194, 2014, 9, Downloaded from https://agupubs.onlinelibrary.wiley.com/doi/10.1002/2014TC003593 by National Medical Library The Director, Wiley Online Library on [21/11/2022]. See the Terms and Conditions (https://onlinelibrary.wiley.com/terms-and-conditions) on Wiley Online Library for rules of use; OA articles are governed by the applicable Creative Commons License

main foliation; D3, brittle-ductile faults with minor displacement; and D4, brittle faults. Rocks on this flank of the dome that contain the D1 foliation and stretching lineation record top-down-to-the-W shear sense (Figures 2 and 4), and they are intruded by deformed and undeformed leucogranite bodies (Figure 4). Based on location within the LPD and the structural level of the LPSZ, we separate the LPD into five domains (Figure 2). The Chango and Sumdo transects contain rocks of the Haimanta Group within the uppermost structural positions of the LPSZ. The south and central domains contain rocks of the Haimanta Group from intermediate depths within the LPSZ. The east domain contains migmatite and gneiss that potentially underlie the Haimanta Group and represent the deepest structural positions of the LPSZ. Near the villages of Chango and Sumdo, rocks within the Chango and Sumdo transects are in the hanging wall of the Kaurik-Chango normal fault (Figure 2).

The rocks in the Chango and Sumdo transects contain a foliation and stretching lineation that were folded into a low-amplitude, NE trending anticline (Figures 2 and 3). Folding rotated the stretching lineations to an E-W trend with opposite plunges (Figures 2b and 2c). Mesoscale shear bands on the west limb record top-down-to-the-W shear. Biotite to garnet grade metamorphic rocks in the Chango and Sumdo transects transition to sedimentary rocks in the hanging wall of the LPSZ that range between unmetamorphosed to low grade (Figure 2).

In the central domain, the LPSZ is defined by a west dipping foliation and downdip stretching lineation (Figure 2d). Mesoscopic shear sense indicators such as shear bands record top-down-to-the-W shear sense (Figures 4e to 4g). An outcrop of quartzite and marble in the central domain contains a penetrative lineation without a foliation, indicating an L-tectonite fabric that formed during heterogeneous strain distribution in this portion of the shear zone (Figures 4c and 4d).

Like the central domain, the southern domain contains a west dipping foliation and approximately downdip stretching lineation. Mesoscopic shear sense indicators, such as shear bands, record top-down-to-the-W shear sense. However, the rocks in the southern domain transition toward the south into rocks that are not intruded by leucogranite and do not record shear sense associated with the LPSZ (M. Jessup et al., in review, 2014).

The east domain contains rocks that represent the structurally deepest positions in the dome and contain a SE dipping foliation and E trending shallow stretching lineation (Figure 2f). Mesoscopic shear bands in migmatitic gneiss suggest a transition to top-down-to-the-east shear sense on this side of the dome [*Langille et al*., 2012]. Mesoscale observations and samples for this portion of the dome are limited due to the remoteness of the region.

4.2. Microscale Observations

4.2.1. Description of Samples

Samples collected from the LPSZ in the Sumdo transect are fine-grained phyllite with quartz, biotite, muscovite, and minor iron oxides that transition to schist dominated by fine-grained quartz and biotite at deeper structural depths (Figure 5a). The Chango transect contains samples that transition from undeformed or weakly deformed limestone and marble to biotite garnet schist within the shear zone (Table 1). Samples from the shear zone contain relatively coarser quartz (~100 μm) with biotite, muscovite, chlorite, sparse, and fine-grained feldspar and ~500–1000 μm garnet porphyroclasts (Figure 5b). Samples from the central domain were taken from the schist, quartzite, and marble of the host rock and from leucogranite intrusions. The schist is similar to that in the Chango transect with the addition of kyanite and staurolite porphyroclasts. The quartzite is relatively pure with minor amounts of biotite and muscovite (Figure 5c). The leucogranite is quartz dominated with coarse feldspar porphyroclasts throughout (Figure 5d). Schist samples from the southern domain are similar to those from the central domain but contain sillimanite ± cordierite (Figure 5e). The eastern domain contains gneiss with quartz, feldspar, muscovite, biotite, and sillimanite ± garnet and amphibole porphyroclasts (Figure 5f).

4.2.2. Kinematic Observations

Microstructures in rocks from all of the domains were evaluated to determine the kinematic evolution of the LPSZ. With the exception of rocks in the east domain, top-down-to-the-W fabrics dominate throughout each domain that we investigated. Microscopic shear sense indicators in rocks from the Chango and Sumdo transects include strain shadows on porphyroclasts, shear bands, and mica fish that consistently indicate top-down-to-the-W shear sense (Figures 5a and 5b and Table 1). In the Sumdo transect, rocks in the hanging wall of the LPSZ transition to metasedimentary rocks with a weak lineation and foliation. Microscopic shear sense indicators in rocks from the central and southern domains include strain shadows on rigid

©2014. American Geophysical Union. All Rights Reserved.

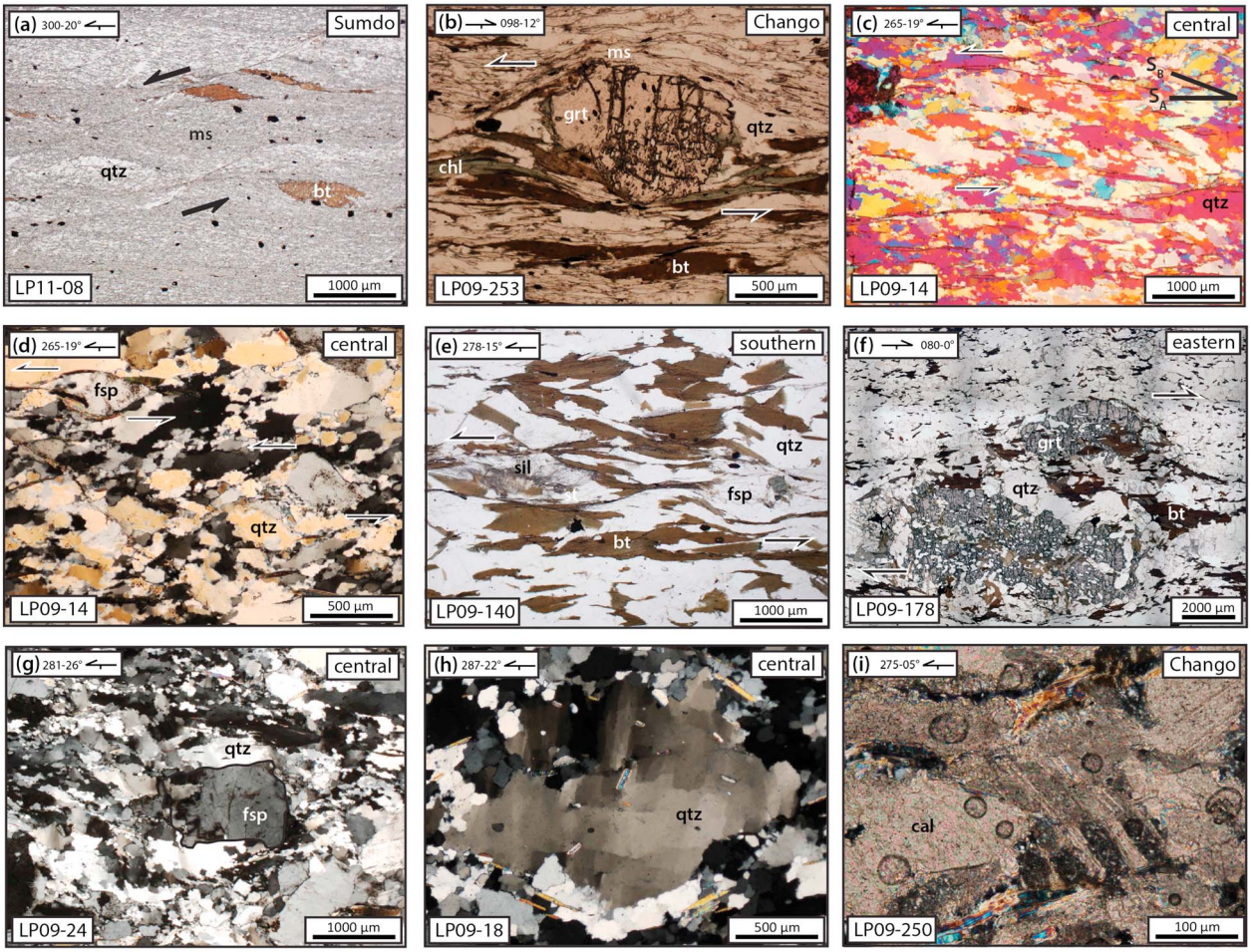

Figure 5. Photomicrographs of representative samples from each of the domains of the Leo Pargil dome. (a) Biotite (bt) fish and shear bands indicating top-down-to-the-NW shear sense: qtz, quartz; ms, muscovite. (b) Strain shadow on garnet (grt) porphyroclast suggesting top-down-to-the-W shear sense: chl, chlorite. (c) Oblique quartz fabric exhibiting grains that preserve grain boundary migration recrystallization (GBM) suggesting top-down-to-the-W shear sense at temperatures of >500°C. (d) Quartz recording GBM and deformed feldspars (fsp) suggesting top-down-to-the-W shear sense and temperatures of >500°C. (e) Rotated feldspar and sillimanite suggest top-down-to-the-W shear sense. (f) Strain shadow on garnet clasts indicates E directed shear. (g) Quartz exhibiting GBM and a feldspar grain (outlined in black for clarity) with subgrain rotation recrystallization suggesting temperatures of >600°C. (h) Checkerboard extinction in quartz indicating >650°C. (i) Type IV calcite (cal) twins surrounded by other calcite grains that have been completely recrystallized at temperatures of >300°C.

porphyroclasts, quartz oblique fabrics, and shear bands. These microstructures record top-down-to-the-W shear sense (Figures 5c to 5e and Table 1). Rocks in the east domain, from the structurally deepest position in the dome, contain shear bands and strain shadows on garnet porphyroclasts that record top-down-to-the-E shear sense (Figure 5f and Table 1), consistent with mesoscale shear sense indicators.

5. Temperatures and Kinematics During Deformation

5.1. Methods for Estimating Deformation Temperatures

The temperatures that were reached during top-down-to-the-W shearing were estimated using (1) recrystallized quartz and feldspar microstructures [*Hirth and Tullis*, 1992; *Fitz Gerald and Stünitz*, 1993; *Stipp et al*., 2002a, 2002b], (2) quartz slip systems determined from quartz lattice-preferred orientation (LPO) patterns [e.g., *Mainprice et al*., 1986], (3) the opening angle of quartz [c] axis LPO patterns [*Kruhl*, 1998; *Law et al*., 2004], and (4) calcite twins [e.g., *Weber et al*., 2001; *Ferrill et al*., 2004].

Quartz exhibits bulging recrystallization (BLG) at temperatures of 280–400°C, subgrain rotation recrystallization (SGR) at 400–500°C, and grain boundary migration recrystallization (GBM) at >500°C (Figures 5c, 5d, and 5g) [*Stipp et al*., 2002a, 2002b]. At >650°C, quartz begins to develop checkerboard

©2014. American Geophysical Union. All Rights Reserved.

19449194, 2014, 9, Downloaded from https://agupubs.onlinelibrary.wiley.com/doi/10.1002/2014TC003593 by National Medical Library The Director, Wiley Online Library on [21/11/2022]. See the Terms and Conditions (https://onlinelibrary.wiley.com/terms-and-conditions) on Wiley Online Library for rules of use; OA articles are governed by the applicable Creative Commons License

Table 1. Summary of Kinematic and Deformation Temperature Data[a]

Sample	Rock Type	Shear Sense	Shear Sense Indicators	Deformation Temperature (°C)	Temperature Indicator
			Sumdo transect		
Hanging wall					
LP09-274	Phyllite	Top-60	Mica fish, shear bands	<280	Rigid quartz
LP09-270	Phyllite	Top-093	Mica fish, shear bands	~280	Onset of BLG in quartz
LP09-267	Calc-silicate	—	—	200–300	Type II calcite twins
Footwall					
LP11-08	Schist	Top-300	Mica fish, shear bands	400–500	Quartz SGR
LP09-264	Schist	Top-230	Shear bands	400–450	Quartz SGR, rigid feldspar
LP11-01	Schist	Top-200	Shear bands	400–500	Quartz SGR
LP11-07	Schist	Top-250	Strain shadows	400–450	Quartz SGR, rigid feldspar
LP11-05	Schist	Top-220	Mica fish	400–450	Quartz SGR, rigid feldspar
LP11-06	Schist	Top-255	Strain shadows	400–450	Quartz SGR, rigid feldspar
			Chango transect		
Hanging wall					
LP09-113	Limestone	—	—	—	—
LP09-91	Marble	—	—	200–300	Type II calcite twins
Footwall					
LP09-94	Schist	Top-260	Shear bands	400–500	Quartz SGR
LP09-102	Schist	Top-270	Shear bands	400–450	Quartz SGR[b], rigid feldspar
LP09-98	Schist	Top-225	Shear bands	400–450	Quartz SGR[b], rigid feldspar
LP09-253	Schist	Top-278	Shear bands, strain shadows	400–450	Quartz SGR[b], rigid feldspar
			Central domain		
LP09-191[c]	Quartzite	Top-286	Oblique fabric, mica fish, LPO	500–650	Quartz GBM, prism < a >
LP09-222[c]	Leucogranite	Top-210	Oblique fabric, strain shadows, LPO	>650	Quartz checkerboard extinction, prism [c]
LP09-24[c]	Leucogranite	Top-281	Oblique fabric, tails, mica fish, LPO	600–650	Quartz GBM, feldspar SGR, prism < a >
LP09-21[c]	Quartzite	Top-268	Oblique fabric, mica fish	500–650	Quartz GBM, prism < a >
LP09-18	Quartzite	Top-287	Oblique fabric, mica fish	>650	Quartz checkerboard extinction
LP09-14[c]	Quartzite	Top-265	Oblique fabric, strain shadows, mica fish, LPO	600–650, 670 ± 30	Quartz GBM, feldspar SGR, opening angle
LP09-76	Schist	Top-300	Shear bands, strain shadows	500–650	Quartz GBM
LP09-229	Schist	Top-273	Shear bands, strain shadows	500–650	Quartz GBM
LP09-79	Schist	Top-290	Shear bands, strain shadows	500–650	Quartz GBM
LP09-263	Schist	Top-270	Shear bands	500–650	Quartz GBM
			Southern domain		
LP09-140	Schist	Top-287	Shear bands, strain shadows	600–650	Quartz GBM, feldspar SGR
LP09-175	Schist	Top-270	Tails	600–650	Quartz GBM, feldspar SGR
LP09-161	Schist	Top-260	Strain shadows	600–650	Quartz GBM, feldspar SGR
			Eastern domain		
LP09-177	Gneiss	Top-081	Shear bands	500–650	Quartz GBM
LP09-178	Gneiss	Top-080	Shear bands, strain shadows	500–650	Quartz GBM
LP09-187	Gneiss	Top-075	Strain shadows	>650	Quartz checkerboard extinction, myrmekite

[a]SGR, subgrain rotation; GBM, grain boundary migration. All samples are from within the shear zone in the footwall unless otherwise specified.
[b]SGR in quartz is overprinted by BLG.
[c]Analyzed with electron backscatter diffraction (EBSD).

extinction (Figure 5h). At <450°C, feldspar is rigid and deforms by brittle fracturing [*Pryer*, 1993]. Dislocation glide (Figure 5d) and BLG recrystallization are possible in feldspar grains at 450–600°C [*Pryer*, 1993]. BLG and SGR recrystallization can occur in feldspar at >600°C (Figure 5g) [*Tullis and Yund*, 1991].

Slip systems within quartz grains that recrystallize during deformation also constrain deformation temperatures. The slip systems are determined from the LPOs of the quartz grains within a sample, viewed in the plane perpendicular to foliation and parallel to lineation (XZ section). The LPOs, when plotted on a stereonet, yield maxima indicative of the slip systems (Figure 6) [e.g., *Lister and Hobbs*, 1980; *Law*, 1990]. Quartz LPOs were obtained using electron backscatter diffraction patterns collected with a FEI Quanta 400 FEG scanning electron microscope coupled with a HKL Nordlys 2 electron backscatter diffraction (EBSD) camera at the University of California, Santa Barbara. CHANNEL 5 HKL software indexed the diffraction patterns with Hough resolution of 80, detecting 7–8 bands with standard divergence and a quartz structure file containing 60 reflectors.

©2014. American Geophysical Union. All Rights Reserved.

19449194, 2014, 5, Downloaded from https://agupubs.onlinelibrary.wiley.com/doi/10.1002/2014TC003593 by National Medical Library The Director, Wiley Online Library on [21/11/2022]. See the Terms and Conditions (https://onlinelibrary.wiley.com/terms-and-conditions) on Wiley Online Library for rules of use; OA articles are governed by the applicable Creative Commons License

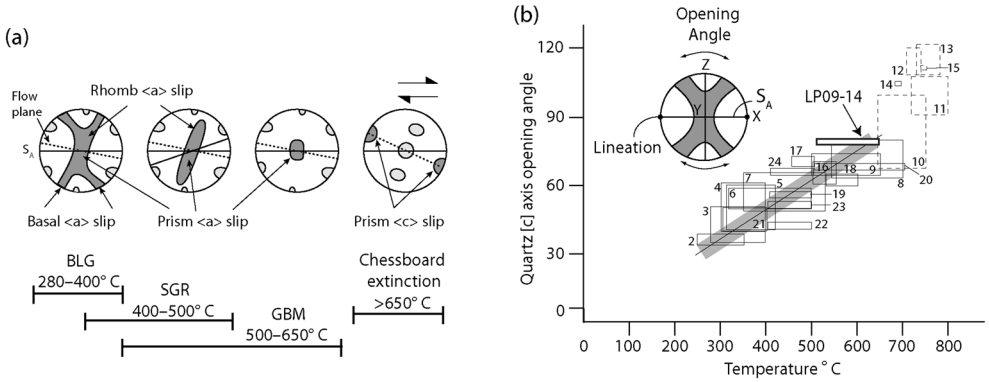

Figure 6. (a) Quartz lattice-preferred orientation (LPO) patterns and slip systems expected for plane strain noncoaxial deformation with increasing temperature (modified from *Passchier and Trouw* [2005] and *Langille et al.* [2010a]). (b) Correlation between opening angle and temperature. Dashed boxes represent data from quartz with prism [c] slip. Boxes 1–15: *Kruhl* [1998]; 16: *Law et al.* [1992]; 17: *Nyman et al.* [1995]; 18: *Okudaira et al.* [1995]; 19 and 20: *Langille et al.* [2010b]; 21–24: *Langille et al.* [2010a]. Opening angle from this study included, plotted against temperatures inferred from quartz and feldspar textures. Modified from *Law et al.* [2004].

Although slip on different systems can occur at a range of temperatures, basal < a > slip is dominant at 280–400°C, prism < a > and rhomb < a > are dominant at 400–500°C, and prism < a > is dominant at 500–650°C. At >650°C, prism [c] becomes dominant [e.g., *Lister and Dornsiepen*, 1982; *Mainprice et al.*, 1986; *Kruhl*, 1998] (Figure 6a). LPO patterns that exhibit basal < a >, prism < a >, and rhomb < a > slip often contain a crossed girdle pattern. The opening angle is defined as the angle between the girdles (Figure 6b) [*Kruhl*, 1998].

Experimental studies [e.g., *Tullis et al.*, 1973; *Lister et al.*, 1978; *Lister and Hobbs*, 1980; *Lister and Dornsiepen*, 1982; *Wenk et al.*, 1989] indicate that the opening angle of quartz [c] axis LPOs increases with increasing deformation temperature (Figure 6b); therefore, it can be used to calculate the deformation temperature [*Kruhl*, 1998]. Previous studies attributed an uncertainty of ± 50°C to the temperature estimate using this method, based on the combined standard deviation of the temperature and opening angle data between 280°C and >650°C [*Kruhl*, 1998]. However, the linear relationship between opening angle and temperature changes at >650°C, when prism [c] slip begins to develop in quartz (Figure 6b). Recalculating the standard deviation of all data in the temperature range between 280°C and 650°C yields an uncertainty of ± 30°C. In addition to temperature, other factors such as strain rate also contribute to the development of the opening angle [*Tullis et al.*, 1973]. However, the compiled data (Figure 6b) represent samples from varying deformation states. Because the correlation between temperature and opening angle is still expressed, factors other than temperature result in a variability that is within the uncertainty assigned to the temperature estimate.

In addition to quartz and feldspar, calcite twins can be indicative of deformation temperatures. Type I twins are characterized by thin lines that develop at <200°C [e.g., *Weber et al.*, 2001; *Ferrill et al.*, 2004]. At 200–300°C, wide bands (type II twins) develop in calcite during dislocation glide [e.g., *Weber et al.*, 2001; *Ferrill et al.*, 2004]. With increasing temperature, the calcite twins obtain curvature (type III) and become patchy (type IV) with the onset of dynamic recrystallization (Figure 5i). Complete dynamic recrystallization occurs at >300°C [e.g., *Weber et al.*, 2001; *Ferrill et al.*, 2004].

5.1.1. Results

Metamorphosed and deformed rocks of the Haimanta Group, exposed within the LPSZ in the Chango and Sumdo transects, transition to low-grade or unmetamorphosed sedimentary rocks in the hanging wall that were undeformed by the shear zone (Figure 2). Quartz and feldspar textures observed within each sample contain little variation between specific microstructural domains and are representative of the textures exhibited throughout the sample. Rocks within these transects in the LPSZ contain quartz that exhibits subgrain rotation and feldspar that remained rigid, suggesting deformation at temperatures of 400–450°C (Table 1). Some samples contain quartz that is overprinted by BLG recrystallization, indicating continued recrystallization through 280–400°C (Table 1). LP09-250 contains calcite that was dynamically recrystallized at temperatures of >300°C (Table 1 and Figure 5i). Toward structurally higher positions in the hanging wall of

©2014. American Geophysical Union. All Rights Reserved.

19449194, 2014, 9, Downloaded from https://agupubs.onlinelibrary.wiley.com/doi/10.1002/2014TC003593 by National Medical Library The Director, Wiley Online Library on [21/11/2022]. See the Terms and Conditions (https://onlinelibrary.wiley.com/terms-and-conditions) on Wiley Online Library for rules of use; OA articles are governed by the applicable Creative Commons License

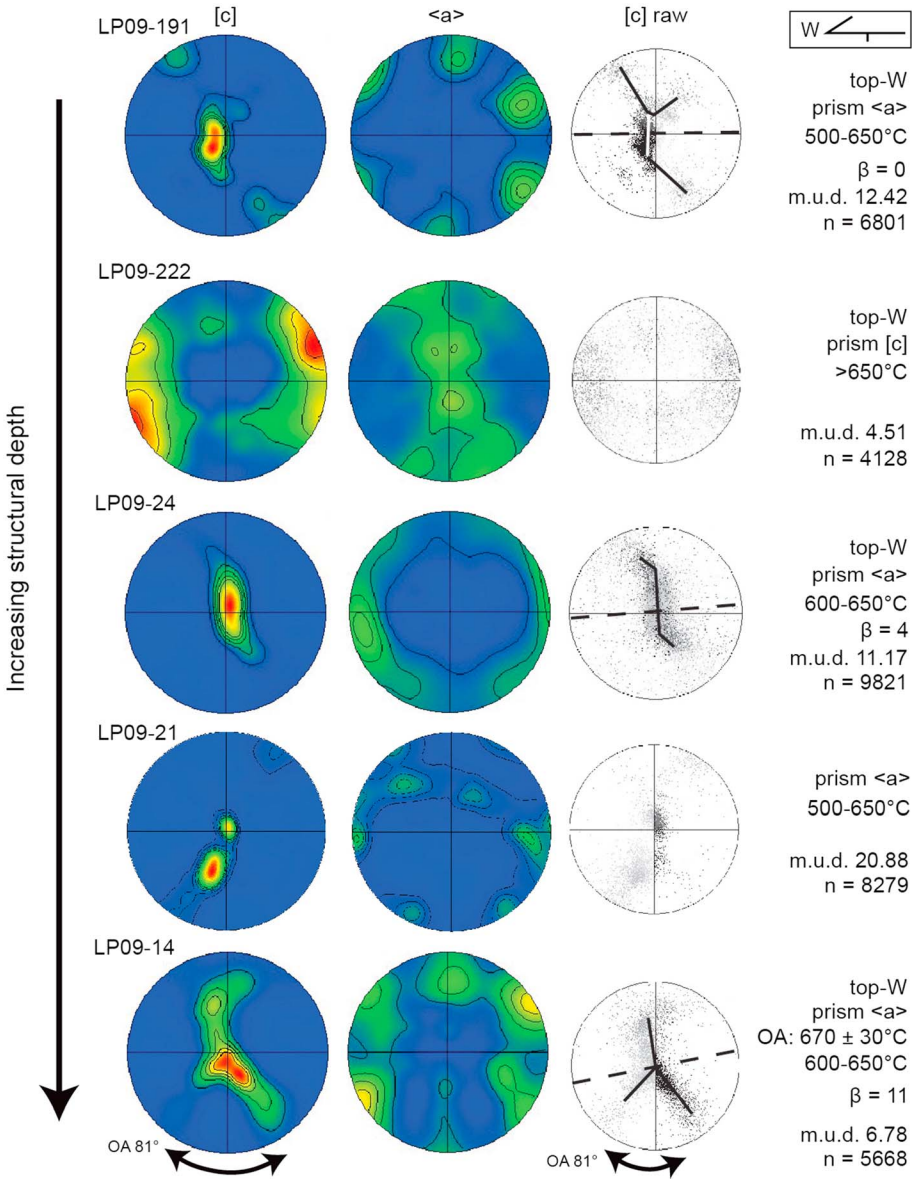

Figure 7. Quartz lattice-preferred orientation (LPO) patterns for deformed quartzite and leucogranite samples from the quartzite unit in the central domain. Dashed line represents the flow plane. The raw [c] axis data are included, and the interpreted pattern skeleton is shown. Interpreted shear sense, dominant slip system, and temperatures determined from quartz and feldspar textures are included: m.u.d., mean uniform distribution; *n* = number of points; OA, opening angle. See Figure 8 for definition of β.

the LPSZ, a transition occurs from quartz with the onset of BLG recrystallization through type II calcite twins and into quartz with primary grains (Table 1).

Metamorphic rocks in the south, central, and eastern domains record deformation at higher temperatures. The south and central domains contain quartz grains that exhibit GBM and feldspar grains that record SGR, suggesting temperatures of 500–650°C (Table 1 and Figure 5g). Checkerboard extinction of quartz in some samples indicates temperatures of >650°C (Figure 5h). Quartz LPO patterns from samples in the central domain dominantly exhibit prism < a > to prism [c] slip, suggesting temperatures of 500–650°C and >650°C, respectively (Figure 7 and Table 1). The LPO pattern of sample (LP09-14) forms a girdle with an opening angle, corresponding to a deformation temperature of 670 ± 30°C (Figure 7 and Table 1). With the exception of LP09-222, LPO-derived temperatures are all within uncertainty of one another,

©2014. American Geophysical Union. All Rights Reserved.

19449194, 2014, 9, Downloaded from https://agupubs.onlinelibrary.wiley.com/doi/10.1002/2014TC003593 by National Medical Library The Director, Wiley Online Library on [21/11/2022]. See the Terms and Conditions (https://onlinelibrary.wiley.com/terms-and-conditions) on Wiley Online Library for rules of use; OA articles are governed by the applicable Creative Commons License

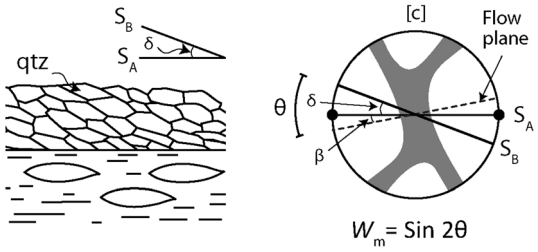

Figure 8. Diagram depicting the aspects used in estimation of vorticity (W_m) from an oblique fabric defined by quartz. S_A is the main foliation, S_B is the oblique quartz fabric, β is the angle between the foliation and flow plane, and δ is the angle between the foliation and the oblique quartz fabric. Modified from *Xypolias* [2009].

presumably because they come from a relatively narrow structural zone within the shear zone. LP09-222 is a sheared leucogranite, and we speculate that the higher apparent temperature recorded in this sample is a result of residual heat from intrusion. Migmatitic gneiss from the eastern transect, in the core of the dome, contains quartz grains that record GBM and/or checkerboard extinction, indicating deformation at 500°C to >650°C (Table 1).

5.2. Methods for Estimating Strain and Vorticity

Vorticity analyses were conducted on three samples from the central domain to quantify the relative contribution of pure shear (coaxial) and simple shear (noncoaxial) during ductile deformation, which can be used to calculate strain ratios that are then used to estimate the relative components of extension and thinning normal to the extension direction. Thinning of crustal material (assuming plane strain) results in higher strain rates, coinciding with an increasing pure shear component [*Law et al*., 2004]. Kinematic vorticity number (W_k) is a measure of the contributions of pure ($W_k = 0$) and simple ($W_k = 1$) shear during steady state deformation. Pure and simple shear components are equal when $W_k = 0.71$ [*Tikoff and Fossen*, 1995; *Law et al*., 2004]. The mean kinematic vorticity number (W_m) is a time-averaged estimate of the bulk vorticity [e.g., *Passchier*, 1987; *Fossen and Tikoff*, 1997, 1998; *Jiang*, 1998]. W_m methods require that deformation progressed under plane strain conditions. However, minor deviations from plane strain may cause an uncertainty [*Tikoff and Fossen*, 1995] that is within the uncertainty associated with conducting vorticity methods. Regardless, these methods were not applied to samples that exhibited L-tectonite fabrics (e.g., constriction; Figure 4c). Furthermore, quartz LPO data for samples that were used to estimate W_m contained LPO fabrics indicative of deformation under plane strain conditions (Figures 6a and 7).

The quartz grain shape foliation technique was applied (Figure 8) [*Wallis*, 1995] to thin sections cut perpendicular to the foliation and parallel to the lineation (XZ section of the finite strain ellipsoid) to estimate W_m. W_m methods using rotating porphyroclasts have come into question as it has been shown that rotation can be decoupled from the matrix material and errors may be significant [e.g., *Johnson et al*., 2009; *Li and Jiang*, 2011]. As opposed to these methods that use rotating porphyroclasts to estimate mean kinematic vorticity, we use oblique quartz fabrics that develop during deformation to estimate W_m.

Quartz grains that recrystallize during deformation are stretched parallel to the instantaneous stretching axis (ISA) [*Wallis*, 1995]. During deformation, quartz grains are predicted to rotate to a maximum angle relative to the flow plane, which approximates the ISA (Figure 8) [*Wallis*, 1995]. The angle between the oblique grain shape fabric (S_B) (Figure 5c) and the flow plane (Figures 6–8) is θ. The flow plane is defined as the perpendicular to the [c] axis girdle of the quartz LPO, where β is the angle between the flow plane and the main foliation (S_A) (Figure 8) [*Law*, 1990; *Wallis*, 1995]. The angle between the oblique grain shape fabric (S_B) and the flow plane is related to W_m by the equation

$$W_m = \sin 2\theta = \sin [2(\delta + \beta)] \quad (1)$$

where δ is the angle between the quartz oblique grain shape fabric (S_B) and S_A (Figure 8) [*Wallis*, 1995].

The long axis of the quartz grains from three samples were measured from images of the thin sections, and the flow planes were measured from quartz LPO patterns (Figure 7). To accurately define the ISA, θ was measured on >100 quartz grains per sample. Constraining θ using the grain shape foliation technique requires a well-developed quartz LPO and oblique grain shape fabric to accurately define the flow plane and the ISA [*Wallis*, 1995; *Xypolias and Koukouvelas*, 2001; *Xypolias*, 2009, 2010]. The β angle from the LPOs was used in our W_m estimates. We followed the method of *Johnson et al*. [2009] by calculating the mean and standard deviation of our θ values to provide a range of W_m estimates for each sample (Figure 9). Additional sources of uncertainty in vorticity values estimated using this technique can be attributed to (1) heterogeneity of the matrix material, (2) the presence of porphyroclasts, and (3) folding—which may all

©2014. American Geophysical Union. All Rights Reserved.

19449194, 2014, 9, Downloaded from https://agupubs.onlinelibrary.wiley.com/doi/10.1002/2014TC003593 by National Medical Library The Director, Wiley Online Library on [21/11/2022]. See the Terms and Conditions (https://onlinelibrary.wiley.com/terms-and-conditions) on Wiley Online Library for rules of use; OA articles are governed by the applicable Creative Commons License

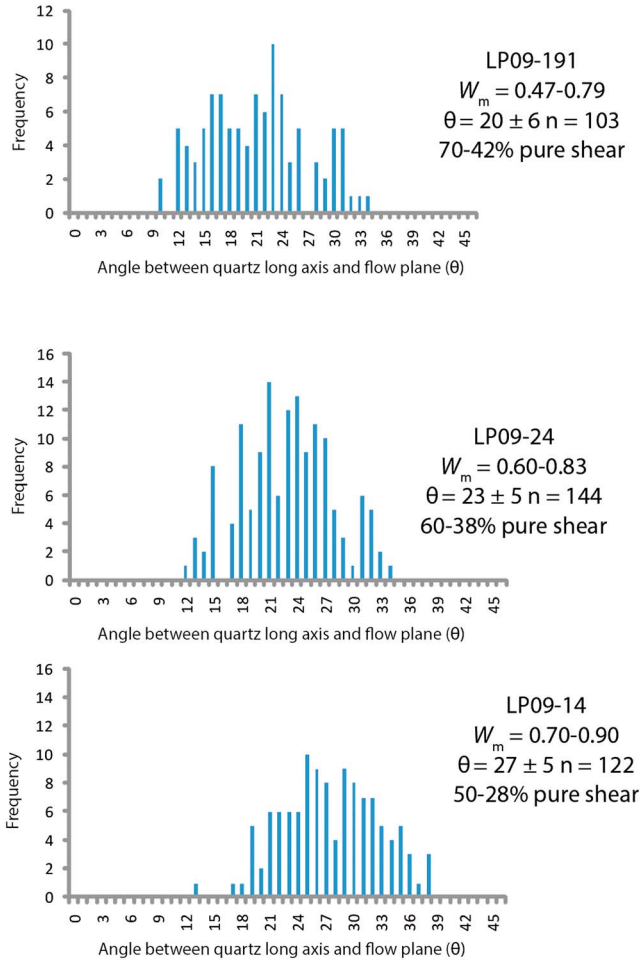

Figure 9. Histograms of quartz grain orientation data and W_m estimates. Refer to Figure 7 for the angle between the flow plane and the main foliation (β).

deflect or influence the orientation and/or development of the quartz fabric. To limit possible inaccuracies, measurements were made from quartz that were apparently unaffected by these interferences.

The strain ratio (R_{xz}) can be calculated from these data using the following equation that utilizes the angular relationships between the quartz oblique grain shape fabrics and quartz [c] axis fabrics [e.g., *Xypolias*, 2009]:

$$R_{xz} = \frac{1 - \tan\theta \times \tan\beta}{\tan^2\beta + \tan\theta \times \tan\beta} \quad (2)$$

where

$$\tan\theta = \cot[2(\beta + \delta)] \quad (3)$$

β is the angle between the flow plane and S_A, as measured from the quartz [c] axis fabric, and δ is the angle between the quartz oblique fabric (S_B) and the main foliation (S_A) (Figure 8). This equation was applied to samples LP09-24 and LP09-14 from the quartzite and marble unit (yellow, Figure 2), and it yielded R_{xz} values from 3 to 18 (Table 2).

The percent downdip extension and shortening normal to the shear plane was calculated from the shortening value (S) using the following equation [*Wallis et al.*, 1993]:

$$S = \left\{0.5\left(1 - W_m^2\right)^{0.5}\left[\left(R_{xz} + R_{xz}^{-1} + \frac{2\left(1 + W_m^2\right)}{\left(1 - W_m^2\right)}\right)0.5 + \left(R_{xz} + R_{xz}^{-1} - 2\right)^{0.5}\right]\right\}^{-1} \quad (4)$$

5.2.1. Results

Quartz grains in three quartzites and quartz-rich leucogranites from the quartzite unit in the central domain of the LPSZ (Figure 2) contain well-developed oblique fabrics. LPO patterns from these samples exhibit maxima from which the flow plane could be determined (Figure 7), making these samples appropriate for W_m analysis using the quartz grain shape foliation technique. These methods yielded W_m estimates of 0.47 to 0.90 (70–28% pure shear), indicating general shear during deformation in this portion of the shear zone (Figure 9 and Table 2).

Using W_m to calculate the strain ratio (R_{xz}) yielded 57 to 164% downdip extension and 36 to 62% shortening normal to extension for two samples (Table 2). The wide range in R_{xz} and S for each sample is attributed to

Table 2. Vorticity and Strain Data

Sample	W_m	% Pure Shear	R_{xz}	% Downdip Extension	% Shortening[a]
LP09-191	0.47–0.79	70–42	—	—	—
LP09-24	0.60–0.83	60–38	9–18	156–164	61–62
LP09-14	0.70-0.90	50–28	3–7	57–61	36–38

[a]Shortening is normal to the downdip direction.

©2014. American Geophysical Union. All Rights Reserved.

19449194, 2014, 9, Downloaded from https://agupubs.onlinelibrary.wiley.com/doi/10.1002/2014TC003593 by National Medical Library The Director, Wiley Online Library on [21/11/2022]. See the Terms and Conditions (https://onlinelibrary.wiley.com/terms-and-conditions) on Wiley Online Library for rules of use; OA articles are governed by the applicable Creative Commons License

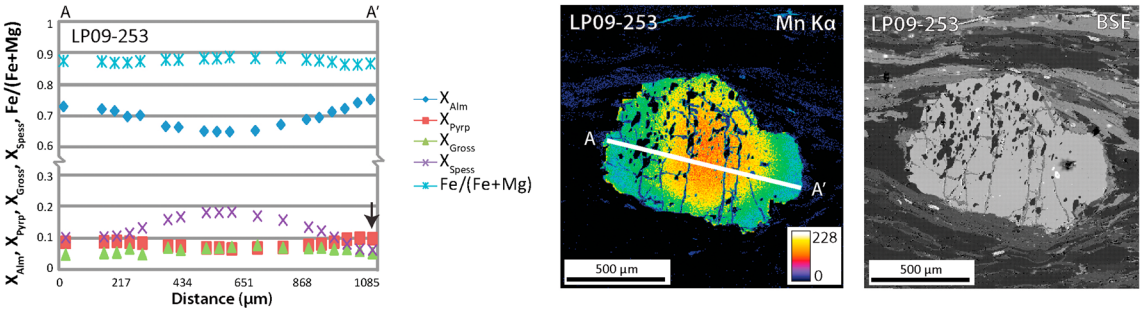

Figure 10. Compositional data from the garnet used for the pressure-temperature estimate. Arrow points to the rim composition used.

thelarge range in W_m values from each sample (Figure 9). The range of R_{xz} and S between samples suggests that strain was partitioned heterogeneously throughout the quartzite/marble unit in this portion of the LPSZ, potentially due to heterogeneities in rheology between the quartzite, marble, and leucogranite in this section. Mesoscale structures of the quartzite in this section contain L-tectonite fabrics associated with constriction (Figure 4c). In lithologically heterogeneous shear zones, constriction may cause folding or boudinage but in rocks that are lithologically homogeneous, such as the section of L-tectonites in the quartzite, L-tectonites form instead [*Sullivan*, 2013]. We interpret constriction to reflect heterogeneous deformation partitioned into this portion of the shear zone, potentially due to lithologic differences between the quartzite and marble in the LPSZ.

6. Thermobarometry

6.1. Methods and Results

An estimate of the P-T conditions at peak temperatures during metamorphism was obtained to evaluate the amount of crustal thickening. The matrix of sample LP09-253 from the Chango transect is composed of biotite, muscovite, quartz, feldspar, and chlorite (after biotite). Garnet in this sample is partially resorbed. Garnet porphyroblasts chosen for analysis showed the least amount of resorption. Chemical data for thermobarometric estimates were acquired using the Cameca SX-100 electron microprobe at the University of Tennessee. X-ray maps using wavelength-dispersive spectrometry of Mg, Mn, and Ca along with

Table 3. Compositional Data (in wt %) for Near-Garnet-Rim Thermobarometric Analyses[a]

	Garnet Near Rim	Biotite	Plagioclase	Muscovite
LP09-253		(18)	(21)	(12)
SiO_2	37.16	35.62	65.87	46.35
TiO_2	0.01	1.64	NA	0.32
Al_2O_3	21.04	18.35	21.73	34.90
FeO	34.00	19.20	0.11	2.21
MnO	3.21	0.14	NA	0.01
MgO	2.72	9.80	NA	0.62
CaO	2.21	0.01	2.51	0.01
Na_2O	0.05	0.20	9.54	1.07
K_2O	NA	9.14	0.08	9.09
Σ	100.40	98.10	99.84	98.58
Si	2.99	5.48	2.89	6.20
Ti	0.00	0.19	NA	0.03
Al	2.00	3.33	1.12	5.50
Fe	2.29	2.47	0.00	0.25
Mn	0.22	0.02	NA	0.00
Mg	0.33	2.25	NA	0.13
Ca	0.19	0.00	0.12	0.00
Na	0.01	0.06	0.81	0.28
K	NA	1.80	0.01	1.55
Σ	8.03	19.59	4.95	17.94

[a]Numbers in parenthesis represent the number of data points averaged. NA = not applicable.

©2014. American Geophysical Union. All Rights Reserved.

19449194, 2014, 9, Downloaded from https://agupubs.onlinelibrary.wiley.com/doi/10.1002/2014TC003593 by National Medical Library The Director, Wiley Online Library on [21/11/2022]. See the Terms and Conditions (https://onlinelibrary.wiley.com/terms-and-conditions) on Wiley Online Library for rules of use; OA articles are governed by the applicable Creative Commons License

quantitative line transects were conducted across garnet porphyroblasts to characterize compositional zonation at 15 kV, 30 nA, 30 ms dwell time, and a 6 μm spot size. To assess compositional heterogeneities of each phase throughout the sample, point analyses at 15 kV, 20 nA, and a spot size of 1 μm were conducted on biotite, plagioclase, and muscovite. Plagioclase was analyzed at 10 kV. Elemental abundances <300 ppm are considered below the detection limit for all elements except *Y* which is ~400 ppm.

The decrease of Mn content from core to rim in garnet indicates prograde zonation (Figure 10). Garnets contain thin (5–10 μm) rims with an increase in Mn as a result of retrograde net transfer reactions [*Kohn and Spear*, 2000]. Biotite, muscovite, and plagioclase had minor compositional variations and were averaged for the P-T estimate (Table 3). These data were combined with the garnet near-rim composition with the lowest Mn value to approximate peak conditions (Figure 10 and Table 3).

P-T estimates at peak temperatures were calculated from the chemical data using THERMOCALC v. 3.33 in the average P-T mode [*Powell et al*., 1998]. Calculations were made using the updated *Holland and Powell* [1998] data set (tc-ds55.txt). Activity coefficients for each phase were calculated using the AX software. No end-members were excluded, as any exclusion resulted in a larger uncertainty. These methods yield 570 ± 105°C and 8.0 ± 1.8 kbar (cor = 0.84 and fit = 0.19).

7. Discussion

7.1. Thermal and Kinematic Evolution of the Leo Pargil Shear Zone

Data obtained in this study are used to evaluate the thermal and kinematic evolution of the LPSZ upon which to build a broader understanding of synconvergent extension in the western Himalaya. In the Sumdo and Chango transects, rocks at the uppermost structural positions within the LPSZ record W directed shearing at ~400–500°C. Rocks within the Chango transect record overprinting through 280–400°C during continued deformation (Table 1). These rocks are overlain by low-grade (<300°C; Figure 3 and Table 1) metasedimentary rocks in the hanging wall of the LPSZ that do not record W directed shearing. Rocks in the Sumdo transect record top-to-the-E shearing in a structural position immediately above the LPSZ where BLG recrystallization occurred (Figure 2 and Table 1). E directed shearing in these rocks is interpreted to record deformation that predates dome formation.

In the Chango transect, Barrovian metamorphism reached 570 ± 105°C and 8.0 ± 1.8 kbar before ending at ~30 Ma [*Langille et al*., 2012]. Assuming a lithostatic pressure gradient of 3.7 km/kbar, this pressure and associated error correspond to ~23–36 km depth. Ductile top-down-to-the-W deformation in the footwall of the LPSZ exhumed these rocks through 400–500°C to 400–280°C. The remaining vertical exhumation likely occurred at <280°C via processes such as erosion and brittle normal displacement on the Kaurik-Chango normal fault system.

P-T data from the southern domain suggest that initiation of the LPSZ occurred during near-isothermal decompression from 630 ± 30°C and 6.6 ± 0.8 kbar during Barrovian metamorphism to 592 ± 32°C and 4.4 ± 0.7 kbar by ~23 Ma [*Langille et al*., 2012]. While the geothermal gradient in the western Himalaya is spatially and temporally variable, the pressure during Barrovian metamorphism suggests these rocks were at a depth of ~22–27 km. When combined with a temperature of ~630 ± 30°C, these data indicate a field gradient of ~22–30 °C/km at this time in a tectonic setting directly associated with dome-forming processes.

Rocks exposed in the central and southern domains record W directed shearing from 500°C to >650°C (Table 1), and they represent deeper structural depths than the rocks exposed in the Chango and Sumdo transects (Figure 3). Deformation temperatures from within the central and southern domains (500°C to >650°C) overlap with metamorphic temperatures for the southern domain during decompression (~600°C), related to the onset of exhumation along the LPSZ and subsequent intrusion of leucogranite [*Langille et al*., 2012; *Lederer et al*., 2013]. This supports decompression concurrently with W directed deformation within a zone of distributed deformation on the LPSZ [*Langille et al*., 2012].

7.2. Tectonics of the Western Himalaya

New data described here indicate that top-down-to-the-W ductile deformation occurred at temperatures of up to > 650°C at the deepest structural positions in the dome, while shallower positions reached 400–500°C. These data are combined with existing data [*Murphy et al*., 2000; *Phillips et al*., 2004; *Lacassin et al*., 2004a;

©2014. American Geophysical Union. All Rights Reserved.

19449194, 2014, 9, Downloaded from https://agupubs.onlinelibrary.wiley.com/doi/10.1002/2014TC003593 by National Medical Library The Director, Wiley Online Library on [21/11/2022]. See the Terms and Conditions (https://onlinelibrary.wiley.com/terms-and-conditions) on Wiley Online Library for rules of use; OA articles are governed by the applicable Creative Commons License

Thiede et al., 2006; *Searle et al*., 2007; *Hintersberger et al*., 2010, 2011; *Langille et al*., 2012] from the western Himalaya to explore potential relationships between the LPSZ and other structures in the western Himalaya and evaluate the exhumation history of the LPD in the context of existing models for synconvergent extension in the Himalaya.

Following initiation of the LPSZ during W directed shearing by 23 Ma [*Langille et al*., 2012], the Leo Pargil and Qusum shear zones record cooling of the LPD between 12 and 16 Ma ($^{40}Ar/^{39}Ar$ and Rb-Sr mica ages of *Zhang et al*. [2000], *Thiede et al*. [2006], and *Thöni et al*. [2012]). A decrease in cooling rate is observed at 10 Ma, based on apatite fission track data from the LPD, and is inferred to coincide with initiation of brittle faulting on N trending normal faults on the southwest flank of the LPD [*Thiede et al*., 2006].

Initiation age, amount of offset, and geologic slip rates reported for the Karakoram fault system are all actively debated. Age estimates for initiation of the Karakoram fault range from 15.7 to 13.7 Ma northwest of Tso Morari [*Phillips et al*., 2004], >18.5 Ma near Tso Morari (Figure 1a) [*Leloup et al*., 2011], 12 Ma in the Ayi Shan region [*Wang et al*., 2012], >25 Ma in the Ayi Shan [*Lacassin et al*., 2004a], active deformation in the late Miocene in the Ayi Shan [*Zhang et al*., 2011], and <29 Ma at Tso Morari [*de Sigoyer et al*., 2004]. At the Gurla Mandhata dome, the southern end of the Karakoram fault offsets the South Kailas thrust by 65 km of right-lateral displacement [*Murphy et al*., 2000]. Since the cessation of movement on the South Kailas thrust occurred at 13 Ma (Figure 1a), the Karakoram fault here initiated at <13 Ma [*Murphy et al*., 2000]. The southeast younging of initiation ages for the Karakoram fault along its southern segment implies that it is a southward propagating system [*Murphy et al*., 2000]. ^{3}He isotope data from the Karakoram fault contain a mantle signature, implying that it is a crust-penetrating structure and has been over the last few million years [*Klemperer et al*., 2013].

Detailed studies of N trending and arc-perpendicular-trending brittle faults in the western Himalaya [*Hintersberger et al*., 2011] proposed that $^{40}Ar/^{39}Ar$ and apatite fission track ages, and strain patterns on these faults, record a transition from arc-perpendicular faults (i.e., LPSZ and D4) that developed in regions of radial expansion due to southward migration of thrusting [*Seeber and Armbruster*, 1984; *Armijo et al*., 1986; *Molnar and Lyon-Caen*, 1989; *Murphy et al*., 2009] to N trending brittle faults that initiated at 10 Ma (i.e., Kaurik-Chango and D6) when extension from the Tibetan Plateau was transferred into the western Himalaya. Beginning at 10 Ma and continuing today [*Thiede et al*., 2006; *Hintersberger et al*., 2011], the southern segment of the Karakoram fault accommodates only a portion of the active E-W displacement from within the Tibetan Plateau while the remainder is accommodated southwest of the Karakoram fault by a system of N trending brittle normal faults, including the brittle faults on the southwest flank of the LPD (Figure 1b) [*Hintersberger et al*., 2010, 2011]. E-W extension on N trending brittle faults overprints the arc-perpendicular faults and shear zones, suggesting that this strain regime developed after the regime dominated by radial spreading [*Hintersberger et al*., 2011].

In the context of the regional deformation events presented by *Hintersberger et al*. [2011], our data support a model where initial ductile deformation in the LPSZ is associated with NE trending (D4) faults/shear zones that continued through 16 Ma [*Thiede et al*., 2006]. These were overprinted by N trending brittle faults at 10 Ma [*Thiede et al*., 2006]. N-S brittle faults (D6) record a transition to a system dominated by extension that propagated from the Tibetan Plateau [*Thiede et al*., 2006; *Hintersberger et al*., 2011]. This would support formation of ductile NW directed shear fabrics at ~16 Ma on the LPSZ to have been controlled by radial expansion [*Murphy et al*., 2009]. The change in tectonic regimes at ~10 Ma could be attributed to the marked decrease in displacement on the Karakoram fault and distribution of stress from the Tibetan plateau into the western Himalaya [*Hintersberger et al*., 2011].

The LPSZ initiated in a region located between strike-slip faulting and extension north of the dome related to the Karakoram fault and shortening south of the dome along the STDS and MCTZ. At 23 Ma, when the LPSZ was in the early stages of ductile W directed deformation, the GHS to the south was being extruded toward the foreland between the STDS above and the MCTZ below [*Vannay and Grasemann*, 2001; *Vannay et al*., 2004; *Chambers et al*., 2009]. Recent studies from the GHS suggest that orogen-parallel extension could have occurred within portions of the GHS during southward extrusion at this time [*Xu et al*., 2013]. This record of midcrustal deformation in the LPD, which involves W directed extension at 23 Ma, may be related to the initial stages of orogen-parallel extension at this time but could reflect localized dome formation that may not necessarily record the onset of orogen-parallel extension accommodated by orogen-perpendicular faults and shear zones at this time [e.g., *Murphy et al*., 2000].

©2014. American Geophysical Union. All Rights Reserved.

19449194, 2014, 9, Downloaded from https://agupubs.onlinelibrary.wiley.com/doi/10.1002/2014TC003593 by National Medical Library The Director, Wiley Online Library on [21/11/2022]. See the Terms and Conditions (https://onlinelibrary.wiley.com/terms-and-conditions) on Wiley Online Library for rules of use; OA articles are governed by the applicable Creative Commons License

19449194, 2014, 9, Downloaded from https://agupubs.onlinelibrary.wiley.com/doi/10.1002/2014TC003593 by National Medical Library The Director, Wiley Online Library on [21/11/2022]. See the Terms and Conditions (https://onlinelibrary.wiley.com/terms-and-conditions) on Wiley Online Library for rules of use; OA articles are governed by the applicable Creative Commons License

7.3. Gneiss Domes in the Himalaya

Gneiss domes across the Himalaya are exhumed as a result of different processes and tectonic settings. With the exception of the syntaxes, previous studies propose that exhumation involved either doming during (1) S directed midcrustal channel flow [e.g., *Beaumont et al*., 2001, 2004] or thrusting over a frontal ramp following S directed crustal flow [e.g., *Lee et al*., 2000, 2004] (the North Himalayan gneiss domes) or (2) orogen-parallel extension [e.g., *Murphy et al*., 2000; *Jessup et al*., 2008] (e.g., Ama Drime massif and Gurla Mandhata dome). Our new data from the LPD provide an opportunity to evaluate the mechanisms responsible for exhumation of the LPD in the broader context of these previous studies of gneiss dome formation in the Himalaya.

The granite-cored North Himalayan gneiss domes (e.g., Mabja, Kangmar, Malashan, and Lhagoi Kangri), between the STDS and the Indus-Tsangpo suture in southern Tibet, expose midcrustal rocks and granite that correlate to the midcrustal GHS exposed south of the STDS [*Burg and Chen*, 1984; *Chen et al*., 1990; *Lee et al*., 2000, 2004; *Aoya et al*., 2005, 2006; *Quigley et al*., 2006, 2008; *Lee and Whitehouse*, 2007; *Yan et al*., 2011]. Data from the Mabja and the Kangmar domes [*Lee et al*., 2000, 2004] suggest that the rocks exposed within the North Himalayan gneiss domes originated from within a midcrustal channel where they were deformed during movement on the top-down-to-the-N STDS above and the top-up-to-the-S MCTZ below. Several models have been proposed to explain how these rocks from the midcrustal channel were exhumed and domed. In one model, doming of the midcrustal channel during S directed extrusion exhumed the North Himalayan gneiss domes [e.g., *Beaumont et al*., 2001, 2004]. The second model, based on data from the Mabja and Kangmar domes, suggests that rocks were brought to the surface through thrust faulting along a frontal ramp on the Gyirong-Kangmar thrust, following S directed midcrustal extrusion of the GHS [e.g., *Lee et al*., 2000, 2004]. In the third model, granite within the Malashan gneiss dome was generated during the transition from crustal thickening to extension along the STDS [*Aoya et al*., 2005]. The generation of magma and ascent within the crust in southern Tibet weakened the crust and triggered extension on the STDS. Extension resulted in decompression-driven melting that enhanced further melting [*Aoya et al*., 2005]. While the Malashan gneiss dome shares some similarities to the other North Himalayan gneiss domes, the process of partial melting and midcrustal flow is linked to the formation of this gneiss dome.

Two characteristics of the LPD are inherently different than the North Himalayan gneiss domes: (1) exhumation involved W directed synconvergent extension and (2) there is no evidence for SW directed thrusting or flow in the rocks within the dome. Although the LPD is located north of the STDS and exposes midcrustal rocks that record crustal thickening similar to the North Himalayan gneiss domes, our data from the southwest side of the dome suggest that the rocks within the LPD record a ductile top-down-to-the-W fabric that developed by 23 Ma. Exhumation occurred in a transitional zone between displacement along the STDS to the south and the right-lateral strike-slip faulting on the Karakoram fault to the north. Similar to the Malashan gneiss dome [*Aoya et al*., 2005], early melting during crustal thickening within the LPD (28 Ma to $>$23 Ma) created a weakened crust [*Langille et al*., 2012]. The weakened crust resulted in initiation of the W directed LPSZ by 23 Ma. Extension triggered decompression melting which enhanced melting that continued until 18 Ma [*Lederer et al*., 2013].

Another mechanism that has been attributed to dome formation in the Himalaya involves orogen-parallel extension [e.g., *Murphy et al*., 2002; *Thiede et al*., 2006; *Jessup et al*., 2008]. This process has been proposed for the development of N-S striking normal faults and exhumation of young metamorphic domes in the central Himalaya, such as the Ama Drime massif. The Ama Drime massif is located south of the Lhagoi Kangri and Mabja domes, ~50 km east of Everest. Although it is spatially located near the North Himalayan gneiss domes, the processes that exhumed this dome are different [*Jessup et al*., 2008; *Cottle et al*., 2009; *Langille et al*., 2010a; *Kali et al*., 2010]. The massif is bounded by the W directed Ama Drime detachment on the west side and the E directed Nyönno Ri detachment on the east side [*Jessup et al*., 2008]. These detachments accommodated orogen-parallel extension beginning at ~13 Ma [*Jessup et al*., 2008; *Kali et al*., 2010] and offset the STDS, suggesting that movement on the STDS here had ceased by this time [*Jessup and Cottle*, 2010]. To the north, the Nyönno Ri detachment transitions into the Xaina-Dinggyê graben that is kinematically linked to E-W extension in the interior of the plateau [*Taylor et al*., 2003; *Jessup and Cottle*, 2010]. Unlike the structurally deeper, higher-temperature portion of the LPSZ, the detachments that bound the Ama Drime massif are discrete and occur within a ~300 m wide zone. These detachments exhumed the midcrustal rocks in the footwall with ~21–42 km of displacement on the Ama Drime detachment [*Langille et al*., 2010a].

©2014. American Geophysical Union. All Rights Reserved.

19449194, 2014, 9, Downloaded from https://agupubs.onlinelibrary.wiley.com/doi/10.1002/2014TC003593 by National Medical Library The Director, Wiley Online Library on [21/11/2022]. See the Terms and Conditions (https://onlinelibrary.wiley.com/terms-and-conditions) on Wiley Online Library for rules of use; OA articles are governed by the applicable Creative Commons License

The LPD and Ama Drime massif are similar in that exhumation of these gneiss domes occurred by ductile extension along faults oriented perpendicular to the orogenic front. In contrast to extension in the central Himalaya where convergence is normal (i.e., perpendicular to the orogenic front), initial extension on the LPSZ was potentially transferred from the Karakoram fault within a zone of oblique convergence. These ductile, NE trending normal faults that bound the LPD were overprinted by N-S trending normal faults that record the transition to E-W extension, potentially dominated by extension transferred from the plateau [*Hintersberger et al*., 2010, 2011]. The kinematic setting of the western Himalaya is dominated by a transtensional regime that evolved over time during spatial and temporal variability that resulted exhumation of the LPD.

These differences in the timing, kinematics, and tectonic setting control what processes actually drive gneiss dome formation in the Himalaya. However, constraints from the LPD demonstrate that the tectonic setting can evolve over the exhumation history of the gneiss dome and induce different processes attributed to exhumation of the dome.

8. Conclusions

This study demonstrates that synconvergent extension in the NW Himalaya is a product of spatial and temporal variations in the tectonic regime. Kinematic data from the LPSZ, on the southwest flank of the LPD, suggest that the rocks now exposed in the dome were thinned by up to 62% during ductile top-down-to-the-W displacement within the LPSZ. Geothermobarometric data suggest that midcrustal rocks exposed within the LPSZ were exhumed from depths of ~36 to 22 km since ~23 Ma. This early tectonic regime of doming was progressively overprinted by NE trending shear zones and normal faults at 16 Ma, potentially during radial spreading, then by N trending normal faults at 10 Ma as strain accommodation on the Karakoram fault decreased [*Thiede et al*., 2006; *Hintersberger et al*., 2011]. In contrast to other gneiss domes across the Himalaya, exhumation of the LPD occurred during a temporal transition in tectonic setting from a system dominated by radial spreading to one where deformation was predominantly accommodated southwest of the Karakoram fault [*Thiede et al*., 2006; *Hintersberger et al*., 2011].

Acknowledgments

Thanks to J. Geissman, T. Ehlers, and N. Niemi for editorial comments and to D. Grujic, S. Johnson, and two anonymous reviewers whose comments and reviews strengthened the manuscript. A. Patchen provided assistance with the microprobe at the University of Tennessee. G. Seward provided assistance with the EBSD equipped SEM at the University of California, Santa Barbara. G. Lederer from the University of California, Santa Barbara, P. E. Lee from the University of Tennessee Knoxville, and P. Langille provided field assistance. T. Conner completed a portion of this study as part of his undergraduate research project. Funding for this project was provided by the National Science Foundation grants (EAR-0911561 and EAR-0911416) awarded to M. Jessup and J. Cottle. Funding supporting a 2011 field season was provided by grants and awards from the Department of Earth and Planetary Sciences at the University of Tennessee, ExxonMobil, Sigma Xi, and the Mayo Educational Foundation awarded to J. Langille. All data for this paper are presented within the text.

References

Aoya, M., S. Wallis, K. Terada, J. Lee, T. Kawakami, Y. Weng, and M. Heizler (2005), North-south extension in the Tibetan crust triggered by granite emplacement, *Geology*, *33*, 853–856.

Aoya, M., S. Wallis, T. Kawakami, J. Lee, Y. Wang, and H. Maeda (2006), The Malashan gneiss dome in south Tibet: Comparative study with the Kangmar dome with special reference to kinematics of deformation and origin of associated granites, in *Channel Flow, Ductile Extrusion and Exhumation in Continental Collision Zones*, edited by R. D. Law, M. P. Searle, and L. Godin, *Geol. Soc. London Spec. Publ.*, *268*, 471–495.

Armijo, R., P. Tapponnier, J. L. Mercier, and T. L. Han (1986), Quaternary extension in southern Tibet: Field observations and tectonic implications, *J. Geophys. Res.*, *91*, 13,803–13,872, doi:10.1029/JB091iB14p13803.

Banerjee, P., R. Bürgmann, B. Nagarajan, and E. Apel (2008), Intraplate deformation of the Indian subcontinent, *Geophys. Res. Lett.*, *35*, L18301, doi:10.1029/2008GL035468.

Beaumont, C., R. Jamieson, M. Nguyen, and B. Lee (2001), Himalayan tectonics explained by extrusion of a low-viscosity crustal channel coupled to focused surface denudation, *Nature*, *414*, 738–742.

Beaumont, C., R. Jamieson, M. Nguyen, and S. Medvedev (2004), Crustal channel flows: 1. Numerical models with applications to the tectonics of the Himalayan-Tibetan orogen, *J. Geophys. Res.*, *109*, B06406, doi:10.1029/2003JB002809.

Bettinelli, P., J. P. Avouac, M. Flouzat, F. Jouanne, L. Bollinger, P. Willis, and G. Chitrakar (2006), Plate motion of India and interseismic strain in the Nepal Himalaya from GPS and DORIS measurements, *J. Geod.*, *80*(8), 567–589.

Blisniuk, P. M., B. R. Hacker, J. Glodny, L. Ratschbacher, S. Bi, Z. Wu, M. O. McWilliams, and A. Calvert (2001), Normal faulting in central Tibet since at least 13.5 Myr ago, *Nature*, *412*(6847), 628–632.

Burg, J., and J. Chen (1984), Tectonics and structural zonation of southern Tibet, China, *Nature*, *311*, 219–223.

Catlos, E., M. Harrison, M. Kohn, M. Grove, F. Ryerson, C. Manning, and B. Upreti (2001), Geochronologic and thermobarometric constraints on the evolution of the Main Central Thrust, central Nepal Himalaya, *J. Geophys. Res.*, *106*(B8), 16,177–16,204, doi:10.1029/2000JB900375.

Chambers, J. A., M. Caddick, T. W. Argles, M. S. A. Horstwood, S. Sherlock, N. B. Harris, R. R. Parrish, and T. Ahmad (2009), Empirical constraints on extrusion mechanisms from the upper margin of an exhumed high-grade orogenic core, Sutlej Valley, NW India, *Tectonophysics*, *477*, 77–92.

Chen, Z., K. Hodges, B. Burchfield, L. Royden, and C. Deng (1990), The Kangmar dome: A metamorphic core complex in southern Xizang (Tibet), *Science*, *250*, 1552–1556.

Coleman, M., and K. V. Hodges (1995), Evidence for Tibetan Plateau uplift before 14 Myr ago from a new minimum age for east-west extension, *Nature*, *374*(6517), 49–52.

Cottle, J. M., M. Jessup, D. Newell, S. Horstwood, S. Noble, R. Parrish, D. Waters, and M. Searle (2009), Geochronology of granulitized eclogite from the Ama Drime massif: Implications for the tectonic evolution of the South Tibetan Himalaya, *Tectonics*, *28*, TC1002, doi:10.1029/2008TC002256.

de Sigoyer, J., S. Guillot, and P. Dick (2004), Exhumation of the ultrahigh-pressure Tso Morari unit in eastern Ladakh (NW Himalaya): A case study, *Tectonics*, *23*, TC3003, doi:10.1029/2002TC001492.

©2014. American Geophysical Union. All Rights Reserved.

Dézes, P., J. Vannay, A. Steck, F. Bussy, and M. Cosca (1999), Synorogenic extension: Quantitative constraints on the age and displacement of the Zanskar Shear Zone (northwest Himalaya), *Geol. Soc. Am. Bull.*, *111*, 364–374.
Ferrill, D. A., A. P. Morris, M. A. Evans, M. Burkhard, R. H. Groshong Jr., and C. M. Onasch (2004), Calcite twin morphology: A low-temperature deformation geothermometer, *J. Struct. Geol.*, *26*(8), 1521–1529.
Fitz Gerald, J., and H. Stünitz (1993), Deformation of granitoids at low metamorphic grades. I: Reactions and grain size reduction, *Tectonophysics*, *221*, 269–297.
Fossen, H., and B. Tikoff (1997), Forward modeling of non-steady-state deformations and the 'minimum strain path', *J. Struct. Geol.*, *19*, 987–996.
Fossen, H., and B. Tikoff (1998), Forward modeling of non-steady-state deformations and the 'minimum strain path': Reply, *J. Struct. Geol.*, *20*, 979–981.
Frank, W., B. Grasemann, P. Guntli, and C. Miller (1995), Geological map of the Kishtwar-Chambu-Kulu region (NW Himalayas, India), *Jahrb. Geol. Bundesanst.*, *138*, 299–308.
Gansser, A. (1981), The geodynamic history of the Himalaya, *Geodyn. Ser.*, *3*, 111–121.
Grasemann, B., H. Fritz, and J. C. Vannay (1999), Quantitative kinematic flow analysis from the Main Central Thrust Zone (NW-Himalaya, India): Implications for a decelerating strain path and the extrusion of orogenic wedges, *J. Struct. Geol.*, *21*(7), 837–853.
Grujic, D., M. Casey, C. Davidson, L. Hollister, R. Kundig, T. Pavlis, and S. Schmid (1996), Ductile extrusion of the Higher Himalayan Crystalline in Bhutan: Evidence from quartz microfabrics, *Tectonophysics*, *260*(1-3), 21–43.
Grujic, D., L. S. Hollister, and R. R. Parrish (2002), Himalayan metamorphic sequence as an orogenic channel: Insight from Bhutan, *Earth Planet. Sci. Lett.*, *198*(1-2), 177–191.
Harrison, T. M., P. Copeland, W. Kidd, and O. M. Lovera (1995), Activation of the Nyainqentanghla Shear Zone: Implications for uplift of the southern Tibetan Plateau, *Tectonics*, *14*(3), 658–676, doi:10.1029/95TC00608.
Herren, E. (1987), Zanskar shear zone: Northeast-southwest extension within the Higher Himalayas (Ladakh, India), *Geology*, *15*, 409–413.
Hintersberger, E., R. C. Thiede, M. R. Strecker, and B. R. Hacker (2010), East-west extension in the NW Indian Himalaya, *Geol. Soc. Am. Bull.*, *122*(9-10), 1499–1515.
Hintersberger, E., R. C. Thiede, and M. R. Strecker (2011), The role of extension during brittle deformation within the NW Indian Himalaya, *Tectonics*, *30*, TC3012, doi:10.1029/2010TC002822.
Hirth, G., and J. Tullis (1992), Dislocation creep regimes in quartz aggregates, *J. Struct. Geol.*, *14*(2), 145–159.
Holland, T. J. B., and R. Powell (1998), An internally consistent thermodynamic data set for phases of petrological interest, *J. Metamorph. Geol.*, *16*(3), 309–343.
Jessup, M. J., and J. M. Cottle (2010), Progression from south-directed extrusion to orogen-parallel extension in the Southern Margin of the Tibetan Plateau, Mount Everest region, Tibet, *J. Geol.*, *118*(5), 467–486.
Jessup, M. J., D. Newell, J. Cottle, A. Berger, and J. Spotila (2008), Orogen-parallel extension and exhumation enhanced by focused denudation in Arun River gorge, Ama Drime massif, Tibet-Nepal, *Geology*, *36*, 587–590.
Jiang, D. (1998), Forward modeling of non-steady-state deformations and the 'minimum strain path': Discussion, *J. Struct. Geol.*, *20*, 975–977.
Johnson, S., H. Lenferink, N. Price, J. Marsh, P. Koons, D. West Jr., and R. Beane (2009), Clast-based kinematic vorticity gauges: The effect of slip at matrix/clast interfaces, *J. Struct. Geol.*, *31*, 1–18.
Jouanne, F., J. L. Mugnier, J. F. Gamond, P. L. Fort, M. R. Pandey, L. Bollinger, M. Flouzat, and J. P. Avouac (2004), Current shortening across the Himalayas of Nepal, *Geophys. J. Int.*, *157*(1), 1–14.
Kali, E., P. H. Leloup, N. Arnaud, G. Mahéo, D. Liu, E. Boutonnet, J. Van der Woerd, X. Liu, J. Liu-Zeng, and H. Li (2010), Exhumation history of the deepest central Himalayan rocks, Ama Drime range: Key pressure-temperature-deformation-time constraints on orogenic models, *Tectonics*, *29*, TC2014, doi:10.1029/2009TC002551.
Kapp, P., and J. H. Guynn (2004), Indian punch rifts Tibet, *Geology*, *32*(11), 993–996.
Kellett, D. A., D. Grujic, and S. Erdmann (2009), Miocene structural reorganization of the South Tibetan detachment, eastern Himalaya: Implications for continental collision, *Lithosphere*, *1*(5), 259–281.
Klemperer, S. L., B. M. Kennedy, S. R. Sastry, Y. Makovsky, T. Harinarayana, and M. L. Leech (2013), Mantle helium signature implies the Karakoram fault is an active plate boundary, *Earth Planet. Sci. Lett.*, *366*, 59–70, doi:10.1016/j.epsl.2013.01.013.
Kohn, M. J., and F. Spear (2000), Retrograde net transfer reaction insurance for pressure-temperature estimates, *Geology*, *28*, 1127–1130.
Kruhl, J. H. (1998), Reply: Prism- and basal-plane parallel subgrain boundaries in quartz: A microstructural geothermometer, *J. Metamorph. Geol.*, *16*, 142–146.
Lacassin, R., et al. (2004a), Large-scale geometry, offset and kinematic evolution of the Karakorum fault, Tibet, *Earth Planet. Sci. Lett.*, *219*, 255–269.
Lacassin, R., et al. (2004b), Reply to comment on "Large-scale geometry, offset and kinematic evolution of the Karakorum fault, Tibet", *Earth Planet. Sci. Lett.*, *229*, 159–163.
Langille, J., M. Jessup, J. Cottle, D. Newell, and G. Seward (2010a), Kinematics of the Ama Drime Detachment: Insights into orogen-parallel extension and exhumation of the Ama Drime massif, Tibet-Nepal, *J. Struct. Geol.*, *32*, 900–919.
Langille, J., J. Lee, B. Hacker, and G. Seward (2010b), Middle crustal ductile deformation patterns in southern Tibet: Insights from vorticity studies in Mabja Dome, *J. Struct. Geol.*, *32*, 70–85.
Langille, J., M. Jessup, J. Cottle, G. Lederer, and T. Ahmad (2012), Timing of metamorphism, melting, and exhumation of the Leo Pargil dome, northwest India, *J. Metamorph. Geol.*, *30*, 769–791, doi:10.1111/j.1525-1314.2012.00998.x.
Lavé, J., and J. P. Avouac (2000), Active folding of fluvial terraces across the Siwaliks Hills, Himalayas of central Nepal, *J. Geophys. Res.*, *105*(B3), 5735–5770, doi:10.1029/1999JB900292.
Law, R. D. (1990), Crystallographic fabrics: A selective review of their applications to research in structural geology, *Geol. Soc. London Spec. Publ.*, *54*(1), 335–352.
Law, R. D., S. S. Morgan, M. Casey, C. M. Sylvester, and M. Nyman (1992), The Papoose Flat pluton of eastern California: A re-assessment of its emplacement history in the light of new microstructural and crystallographic fabric observations, *Trans. R. Soc. Edinburgh: Earth Sci.*, *83*, 361–375.
Law, R. D., M. P. Searle, and R. L. Simpson (2004), Strain, deformation temperatures and vorticity of flow at the top of the Greater Himalayan Slab, Everest massif, Tibet, *J. Geol. Soc.*, *161*, 305–320.
Lederer, G., J. Cottle, M. Jessup, J. Langille, and T. Ahmad (2013), Time-scales of partial melting in the Himalayan middle crust: Insight from the Leo Pargil dome, northwest India, *Contrib. Mineral. Petrol.*, *166*, 1415–1441.
Lee, J., and M. Whitehouse (2007), Onset of mid-crustal extensional flow in southern Tibet: Evidence from U/Pb zircon ages, *Geology*, *35*, 45–48.

©2014. American Geophysical Union. All Rights Reserved.

19449194, 2014, 5, Downloaded from https://agupubs.onlinelibrary.wiley.com/doi/10.1002/2014TC003593 by National Medical Library The Director, Wiley Online Library on [21/11/2022]. See the Terms and Conditions (https://onlinelibrary.wiley.com/terms-and-conditions) on Wiley Online Library for rules of use; OA articles are governed by the applicable Creative Commons License

Lee, J., B. Hacker, W. Dinklage, Y. Wang, P. Gans, A. Calvert, J. Wan, A. Blythe, and W. McClelland (2000), Evolution of the Kangmar Dome, southern Tibet: Structural, petrologic, and thermochronologic constraints, *Tectonics*, *19*, 872–895, doi:10.1029/1999TC001147.
Lee, J., B. Hacker, and Y. Wang (2004), Evolution of North Himalayan Gneiss Domes: Structural and metamorphic studies in Mabja Dome, southern Tibet, *J. Struct. Geol.*, *26*, 2297–2316.
Lee, J., C. Hager, S. R. Wallis, D. F. Stockli, M. J. Whitehouse, M. Aoya, and Y. Wang (2011), Middle to late Miocene extremely rapid exhumation and thermal reequilibration in the Kung Co rift, southern Tibet, *Tectonics*, *30*, TC2007, doi:10.1029/2010TC002745.
Leech, M. (2008), Does the Karakoram fault interrupt mid-crustal channel flow in the western Himalaya?, *Earth Planet. Sci. Lett.*, *276*, 314–322.
Leloup, P., E. Boutonnet, W. Davis, and K. Hattori (2011), Long-lasting intracontinental strike-slip faulting: New evidence from the Karakoram shear zone in the Himalayas, *Terra Nova*, *23*, 92–99.
Li, C., and D. Jiang (2011), A critique of corticity analysis using rigid clasts, *J. Struct. Geol.*, *33*, 203–219.
Lister, G. S., and U. F. Dornsiepen (1982), Fabric transitions in the Saxony granulite terrain, *J. Struct. Geol.*, *4*(1), 81–92.
Lister, G. S., and B. E. Hobbs (1980), The simulation of fabric development during plastic deformation and its application to quartzite: The influence of deformation history, *J. Struct. Geol.*, *2*(3), 355–370.
Lister, G. S., M. S. Paterson, and B. E. Hobbs (1978), The simulation of fabric development in plastic deformation and its application to quartzite: The model, *Tectonophysics*, *45*, 107–158.
Mainprice, D., J. L. Bouchez, P. Blumenfeld, and J. M. Tubia (1986), Dominant c slip in naturally deformed quartz: Implications for dramatic plastic softening at high temperature, *Geology*, *14*(10), 819–822.
Miller, C., M. Thoni, W. Frank, B. Grasemann, U. Klotzli, P. Guntli, and E. Draganits (2001), The early Palaeozoic magmatic event in the Northwest Himalaya, India: Source, tectonic setting and age of emplacement, *Geol. Mag.*, *138*(3), 237–251.
Mitsuishi, M., S. Wallis, M. Aoya, J. Lee, and Y. Wang (2012), E-W extension at 19 Ma in the Kung Co area, S. Tibet: Evidence for contemporaneous E-W and N-S extension in the Himalayan orogen, *Earth Planet. Sci. Lett.*, *325-326*, 10–20.
Molnar, P., and H. Lyon-Caen (1989), Fault-plane solutions of earthquakes and active tectonics of the Tibetan Plateau and its margins, *Geophys. J. Int.*, *99*, 123–153.
Molnar, P., and P. Tapponier (1975), Cenozoic tectonics of Asia: Effects of a continental collision, *Science*, *189*, 419–426.
Molnar, P., and P. Tapponier (1978), Active tectonics of Tibet, *J. Geophys. Res.*, *83*, 5361–5375, doi:10.1029/JB083iB11p05361.
Murphy, M. A., A. Yin, P. Kapp, T. M. Harrison, D. Lin, and G. Jinghui (2000), Southward propagation of the Karakoram fault system, southwest Tibet: Timing and magnitude of slip, *Geology*, *28*(5), 451–454.
Murphy, M. A., A. Yin, P. Kapp, T. M. Harrison, C. E. Manning, F. J. Ryerson, D. Lin, and G. Jinghui (2002), Structural evolution of the Gurla Mandhata detachment system, Southwest Tibet: Implications for the eastward extent of the Karakoram fault system, *Geol. Soc. Am. Bull.*, *114*(4), 428–447.
Murphy, M. A., J. E. Saylor, and L. Ding (2009), Late Miocene topographic inversion in southwest Tibet based on integrated paleoelevation reconstructions and structural history, *Earth Planet. Sci. Lett.*, *282*, 1–9.
Najman, Y., et al. (2010), Timing of India-Asia collision: Geological, biostratigraphic, and palaeomagnetic constraints, *J. Geophys. Res.*, *115*, B12416, doi:10.1029/2010JB007673.
Ni, J., and M. Barazangi (1985), Active tectonics of the western Tethyan Himalaya above the underthrusting Indian Plate: The upper Sutlej River basin as a pull-apart structure, *Tectonophysics*, *112*, 277–295.
Nyman, M. W., R. D. Law, and S. S. Morgan (1995), Conditions of contact metamorphism, Papoose Flat Pluton, eastern California, USA: Implications for cooling and strain histories, *J. Metamorph. Geol.*, *13*, 627–643.
Okudaira, T., T. Takeshita, I. Hara, and J. Ando (1995), A new estimate of the conditions for transition from basal <a> to prism [c] slip in naturally deformed quartz, *Tectonophysics*, *250*(1-3), 31–46.
Passchier, C. W. (1987), Stable positions of rigid objects in non-coaxial flow—A study in vorticity analysis, *J. Struct. Geol.*, *9*, 679–690.
Passchier, C. W., and R. J. Trouw (2005), *Microtectonics*, Springer, Berlin.
Phillips, R., and M. Searle (2007), Macrostructural and microstructural architecture of the Karakoram fault: Relationship between magmatism and strike-slip faulting, *Tectonics*, *26*, TC3017, doi:10.1029/2006TC001946.
Phillips, R. J., R. Parrish, and M. P. Searle (2004), Age constraints on ductile deformation and long-term slip-rates along the Karakoram fault zone, Ladakh, *Earth Planet. Sci. Lett.*, *226*, 305–319.
Powell, R., T. Holland, and B. Worley (1998), Calculating phase diagrams involving solid solutions via non-linear equations, with examples using THERMOCALC, *J. Metamorph. Geol.*, *16*(4), 577–588.
Pryer, L. (1993), Microstructures in feldspars from a major crustal thrust zone: The Grenville Front, Ontario, Canada, *J. Struct. Geol.*, *15*(1), 21–36.
Quigley, M., Y. Liangjun, L. Xiaohan, C. Wilson, M. Sandiford, and D. Phillips (2006), $^{40}Ar/^{39}Ar$ thermochronology of the Kampa Dome, southern Tibet: Implications for tectonic evolution of the North Himalayan gneiss domes, *Tectonophysics*, *421*, 269–297.
Quigley, M., Y. Liangjun, C. Gregory, A. Corvino, M. Sandiford, M. Wilson, and L. Xiaohan (2008), U/Pb SHRIMP zircon geochronology and T-t-d history of the Kampa Dome, southern Tibet, *Tectonophysics*, *446*, 97–113.
Robinson, A. C. (2009), Evidence against Quaternary slip on the northern Karajorum fault suggests kinematic reorganization at the western end of the Himalayan-Tibetan orogen, *Earth Planet. Sci. Lett.*, *286*, 158–170.
Robinson, A. C., A. Yin, C. E. Manning, T. M. Harrison, S. H. Zhang, and X. F. Wang (2007), Cenozoic evolution of the eastern Pamir: Implications for strain-accommodation mechanisms at the western end of the Himalayan-Tibetan orogen, *Geol. Soc. Am. Bull.*, *119*(7-8), 882–896.
Sanchez, V., M. Murphy, W. Dupré, L. Ding, and R. Zhang (2010), Structural evolution of the Neogene Gar Basin, western Tibet: Implications for releasing bend development and drainage patterns, *Geol. Soc. Am. Bull.*, *122*, 926–945.
Saylor, J., P. DeCelles, G. Gehrels, M. Murphy, R. Zhang, and P. Kapp (2010), Basin formation in the High Himalaya by arc-parallel extension and tectonic damming: Zhada basin, southwestern Tibet, *Tectonics*, *29*, TC1004, doi:10.1029/2008TC002390.
Searle, M. P., and R. J. Phillips (2004), A comment on "Large-scale geometry, offset, and kinematic evolution of the Karakoram fault, Tibet" by R. Lacassin et al. (Earth Planet. Sci. Lett. 219 (2004) 255-69), *Earth Planet. Lett.*, *229*, 155–158.
Searle, M. P., et al. (1987), The closing of Tethys and the tectonics of the Himalaya, *Geol. Soc. Am. Bull.*, *98*, 678–701.
Searle, M. P., R. D. Law, and M. J. Jessup (2006), Crustal structure, restoration and evolution of the Greater Himalaya in Nepal-South Tibet: Implications for channel flow and ductile extrusion of the middle crust, in *Channel Flow, Ductile Extrusion and Exhumation in Continental Collision Zones*, edited by R. D. Law, M. P. Searle, and L. Godin, *Geol. Soc. London Spec. Publ.*, *268*, 355–378.
Searle, M. P., B. Stephenson, J. Walker, and C. Walker (2007), Restoration of the Western Himalaya: Implications for metamorphic protoliths, thrust and normal faulting, and channel flow models, *Episodes*, *30*, 242–257.
Seeber, L., and J. Armbruster (1984), Some elements of continental subduction along the Himalayan front, *Tectonophysics*, *105*, 263–278.

©2014. American Geophysical Union. All Rights Reserved.

19449194, 2014, 9, Downloaded from https://agupubs.onlinelibrary.wiley.com/doi/10.1002/2014TC003593 by National Medical Library The Director, Wiley Online Library on [21/11/2022]. See the Terms and Conditions (https://onlinelibrary.wiley.com/terms-and-conditions) on Wiley Online Library for rules of use; OA articles are governed by the applicable Creative Commons License

Stipp, M., H. Stunitz, R. Heilbronner, and S. Schmid (2002a), Dynamic recrystallization of quartz: Correlation between natural and experimental conditions, in *Deformation Mechanisms, Rheology and Tectonics: Current Status and Future Perspectives*, edited by S. De Meer et al., *Geol. Soc. London Spec. Publ.*, *200*, 171–190.

Stipp, M., H. Stünitz, R. Heilbronner, and S. M. Schmid (2002b), The eastern Tonale fault zone: A 'natural laboratory' for crystal plastic deformation of quartz over a temperature range from 250 to 700°C, *J. Struct. Geol.*, *24*(12), 1861–1884.

Styron, R. H., M. H. Taylor, and M. A. Murphy (2011), Oblique convergence, arc-parallel extension, and the role of strike-slip faulting in the High Himalaya, *Geosphere*, *7*(2), 582–596.

Sullivan, W. (2013), L-tectonites, *J. Struct. Geol.*, *50*, 161–175.

Taylor, M., and A. Yin (2009), Active structures of the Himalayan-Tibetan orogen and their relationships to earthquake distribution, contemporary strain field, and Cenozoic volcanism, *Geosphere*, *5*(3), 199–214.

Taylor, M., A. Yin, F. Ryerson, P. Kapp, and L. Ding (2003), Conjugate strike slip faulting along the Bangong-Nujiang suture zone accommodates coeval east-west extension and north-south shortening in the interior of the Tibetan Plateau, *Tectonics*, *22*(4), 1044, doi:10.1029/2002TC001361.

Thiede, R. C., J. R. Arrowsmith, B. Bookhagen, M. McWilliams, E. R. Sobel, and M. Strecker (2006), Dome formation and extension in the Tethyan Himalaya, Leo Pargil, northwest India, *Geol. Soc. Am. Bull.*, *118*, 635–650.

Thöni, M., C. Miller, C. Hager, B. Grasemann, and M. Horschinegg (2012), New geochronological constraints on the thermal and exhumational history of the Lesser and Higher Crystalline Units in the Kullu-Kinnaur area of Himachal Pradesh (India), *J. Asian Earth Sci.*, *52*, 98–116.

Tikoff, B., and H. Fossen (1995), The limitations of three-dimensional kinematic vorticity analysis, *J. Struct. Geol.*, *17*(12), 1771–1784.

Tullis, J., and R. A. Yund (1991), Diffusion creep in feldspar aggregates: Experimental evidence, *J. Struct. Geol.*, *13*(9), 987–1000.

Tullis, J., J. M. Christie, and D. T. Griggs (1973), Microstructures and preferred orientations of experimentally deformed quartzites, *Geol. Soc. Am. Bull.*, *84*(1), 297–314.

Valli, F., N. Arnaud, P. Leloup, E. R. Sobel, G. Mahéo, R. Lacassin, S. Guillot, H. Li, P. Tapponnier, and Z. Xu (2007), Twenty million years of continuous deformation along the Karakorum fault, western Tibet: A thermochronological analysis, *Tectonics*, *26*, TC4004, doi:10.1029/2005TC001913.

Vannay, J. C., and B. Grasemann (2001), Himalayan inverted metamorphism and syn-convergence extension as a consequence of a general shear extrusion, *Geol. Mag.*, *138*(3), 253–276.

Vannay, J. C., B. Grasemann, M. Rahn, W. Frank, A. Carter, V. Baudraz, and M. Cosca (2004), Miocene to Holocene exhumation of metamorphic crustal wedges in the NW Himalaya: Evidence for tectonic extrusion coupled to fluvial erosion, *Tectonics*, *23*, TC1014, doi:10.1029/2002TC001429.

Wallis, S. R. (1995), Vorticity analysis and recognition of ductile extension in the Sanbagawa belt, SW Japan, *J. Struct. Geol.*, *17*, 1077–1093.

Wallis, S. R., J. P. Platt, and S. D. Knott (1993), Recognition of syn-convergence extension in accretionary wedges with examples from the Calabrian Arc and the Eastern Alps, *Am. J. Sci.*, *293*, 463–495.

Wang, S., C. Wang, R. Phillips, M. Murphy, X. Fiang, and Y. Yue (2012), Displacement along the Karakoram fault, NW Himalaya, estimated from LA-ICP-MS U-Pb dating of offset geologic markers, *Earth Planet. Sci. Lett.*, *337-338*, 156–163.

Weber, J. C., D. A. Ferrill, and M. K. Roden-Tice (2001), Calcite and quartz microstructural geothermometry of low-grade metasedimentary rocks, Northern Range, Trinidad, *J. Struct. Geol.*, *23*(1), 93–112.

Wenk, H. R., G. Canova, A. Molinari, and U. F. Kocks (1989), Viscoplastic modeling of texture development in quartzite, *J. Geophys. Res.*, *94*(B12), 17,895–17,906, doi:10.1029/JB094iB12p17895.

Wesnousky, S. G., S. Kumar, R. Mohindra, and V. C. Thakur (1999), Uplift and convergence along the Himalayan Frontal Thrust of India, *Tectonics*, *18*(6), 967–976, doi:10.1029/1999TC900026.

Wiesmayr, G., and B. Grasemann (2002), Eohimalayan fold and thrust belt: Implications for the geodynamic evolution of the NW-Himalaya (India), *Tectonics*, *21*(6), 1058, doi:10.1029/2002TC001363.

Williams, H., S. Turner, S. Kelley, and N. Harris (2001), Age and composition of dikes in Southern Tibet: New constraints on the timing of extension and its relationship to postcollisional volcanism, *Geology*, *29*, 339–342.

Xu, Z., Q. Wang, A. Pêcher, F. Liang, X. Qi, Z. Cai, H. Li, L. Zeng, and H. Cao (2013), Orogen-parallel ductile extension and extrusion of the Greater Himalaya in the late Oligocene and Miocene, *Tectonics*, *32*, 191–215, doi:10.1002/tect.20021.

Xypolias, P. (2009), Some new aspects of kinematic vorticity analysis in naturally deformed quartzites, *J. Struct. Geol.*, *31*(1), 3–10.

Xypolias, P. (2010), Vorticity analysis in shear zones: A review of methods and applications, *J. Struct. Geol.*, *32*(12), 2072–2092.

Xypolias, P., and I. K. Koukouvelas (2001), Kinematic vorticity and strain patterns associated with ductile extrusion in the Chelmos shear zone (External Hellenides, Greece), *Tectonophysics*, *338*, 59–77.

Yan, D., M. Zhou, P. Robinson, D. Grujic, J. Malpas, A. Kennedy, and P. Reynolds (2011), Constraining the mid-crustal channel flow beneath the Tibetan Plateau: Data from the Nielaxiongbo gneiss dome, SE Tibet, *Int. Geol. Rev.*, *54*, 615–632.

Zhang, J., L. Ding, D. Zhong, and Y. Zhou (2000), Orogen-parallel extension in Himalaya: Is it the indicator of collapse or the product in process of compressive uplift?, *Chin. Sci. Bull.*, *45*(2), 114–120.

Zhang, R., M. Murphy, T. Lapen, S. Sanchez, and M. Heizler (2011), Late Eocene crustal thickening followed by Early-Late Oligocene extension along the India-Asia suture zone: Evidence for cyclicity in the Himalayan orogen, *Geosphere*, *7*(5), 1249–1268.

©2014. American Geophysical Union. All Rights Reserved.

19449194, 2014, 5, Downloaded from https://agupubs.onlinelibrary.wiley.com/doi/10.1002/2014TC003593 by National Medical Library The Director, Wiley Online Library on [21/11/2022]. See the Terms and Conditions (https://onlinelibrary.wiley.com/terms-and-conditions) on Wiley Online Library for rules of use; OA articles are governed by the applicable Creative Commons License